THE INTERMEDIATE WAVELENGTH MAGNETIC ANOMALY FIELD OF THE NORTH PACIFIC AND POSSIBLE SOURCE DISTRIBUTIONS

J.L. LaBrecque[1], S.C. Cande[1], and R.D. Jarrard[2]

[1]Lamont-Doherty Geological Observatory
of Columbia University
Palisades, N.Y. 10964

[2]Arco Oil and Gas Company
Dallas, Texas

Final Report for NASA Grant NAS-5-25891
L-D.G.O. contribution # LDGO-82-4

TABLE OF CONTENTS

LIST OF FIGURES

ABSTRACT

Employing a technique that eliminates external field sources and the effects of strike aliasing, we have extracted from marine survey data the intermediate wavelength magnetic anomaly field for $|B|$ in the North Pacific. A strong correlation exists between this field and the MAGSAT field although we can detect a directional sensitivity in the MAGSAT field. The intermediate wavelength field is correlated to tectonic features. Island arcs appear as positive anomalies of induced origin likely due to variations in crustal thickness. Seamount chains and oceanic plateaus also are manifested by strong anomalies. The primary contribution to many of these anomalies appears to be due to a remanent magnetization.

The source parameters for the remainder of these features are presently unidentified ambiguous. This study indicates that the sea surface field is a valuable source of information for secular variation analysis and the resolution of intermediate wavelength source parameters.

THE INTERMEDIATE WAVELENGTH MAGNETIC ANOMALY FIELD OF THE NORTH PACIFIC AND POSSIBLE SOURCE DISTRIBUTIONS

Introduction

The object of this study is to investigate the feasibility of extracting intermediate wavelength magnetic anomalies of wavelengths between 3000 km and 300 km from total field data acquired in marine magnetic surveys. The long term objectives of the research are to:

(1) determine the distribution of intermediate wavelength anomalies over the world's oceans,

(2) determine the extent to which MAGSAT describes the distribution of these anomalies,

(3) determine the sources of the intermediate wavelength magnetic field.

Examination of the intermediate wavelength magnetic anomaly field of the ocean basins offers the possibility of constraining some of the ambiguities which affect magnetic anomaly analysis over continental areas. For the most part present models for the development of oceanic lithosphere are relatively simple. The age of the oceanic lithosphere is well known and models for the lithospheric structure are simple and supported by an extensive data set. Thermal sources and gradients have been measured and delineated. Furthermore isostatic constraints require a bathymetric expression for bulk changes in lithospheric structure. Therefore, the variables which might determine the magnetic source distribution are relatively well constrainted in oceanic lithosphere.

In the following pages we will describe the techniques which were developed to recover the intermediate wavelength total field anomalies over the North Pacific from marine survey data. We feel that the investigation has been extremely successful though much remains to be done in extending the areas of the study to other oceanic basins and tectonic features. Also, the

sources of the observed intermediate wavelength anomalies must be studied in far greater detail than has been possible with the limited resources available in this pilot study. The technique is capable of successfully separating intermediate wavelength total field anomalies and of providing a high resolution record for secular variation during the period 1960 to 1980. Furthermore, the sea surface data set provides a higher resolution than the MAGSAT field, due to the closer proximity of the sea surface data to the lithospheric source bodies and eliminates the directional or longitudinal attenuation which is characteristic of present processing for the polar orbiting MAGSAT data. The results of the North Pacific study show that the anomalies observed in the MAGSAT and POGO fields are also observable in the sea surface data set and that many of these anomalies can be more strongly associated with tectonic features due to the increased resolution of the sea surface field. The two data sets are complementary, in areas of reduced track density the MAGSAT field provides higher resolution and the MAGSAT data set also records the all important vector field data. In areas of high track density the sea surface data can be used to refine the MAGSAT data processing techniques and also provide further constraints on source models.

Harrison and Carle (1981) recently examined the spectral content of several long profiles over the Pacific and Atlantic oceans. They concluded that intermediate wavelength energy was observable in marine magnetics profiles. Shure and Parker (1981) introduced a caveat in such studies of long profiles. Spectral analyses of long profiles assume that all anomalies are lineated perpendicular to the track. The spectral analyses are therefore highly susceptible to three dimensional anomalies or oblique lineations which fold energy into the longer wavelength portions of the spectrum. For convenience, we assign the term 'strike-aliasing' to this phenomenon. Shure and

Parker (1981) concluded their study by bandpass filtering the magnetic anomaly pattern in an area of the Juan de Fuca Ridge. The area was chosen because of its dense magnetic surveys perpendicular to the strike of the seafloor anomaly pattern. Shure and Parker concluded that intermediate wavelength anomalies were not present within their study area. The MAGSAT field and our study (Figure 12) both show that the region of the Juan de Fuca ridge is a region of subdued magnetic anomalies in the intermediate wavelengths which strike perpendicular to the track direction. Therefore, it cannot be concluded from the Shure and Parker study that strike aliasing is the cause of the observed intermediate wavelength field in sea surface profiles.

Our study is designed to circumvent the problem of 'strike-aliasing' by filtering randomly oriented profiles over large areas. Our technique is similar to one adopted by Nomura (1979) in a study of the North Pacific intermediate wavelength field but differs in methods of external field correction, data density and areal coverage.

Figure 1 shows the results of this study, i.e. the intermediate wavelength total field anomalies obtained from filtered marine anomaly profiles over the North Pacific. Figure 2 displays the MAGSAT anomaly field (Langel et al., 1982) observed at 400 km. above the same region as Figure 1. Though there is some difference between the two fields of Figs. 1 and 2 in the long wavelength regional fields, close examination of the two fields reveals a remarkable correlation which will be discussed later. Figure 3 shows the secular variation of the total field obtained from the marine data set for Epoch 1970. The intermediate wavelength anomaly field displays a strong correlation to bathymetric features (Fig. 4) which will help in the isolation of source bodies and the development of improved analysis techniques for MAGSAT and future satellite magnetic surveys.

The Data Set:

The data set used in preparing the magnetic anomaly maps (Fig. 1 and Fig. 3) were obtained from Lamont-Doherty data files and the National Geophysical and Solar Terrestrial Data Center (NGSDC). No aeromagnetic data were utilized. The data set consists of 370 ships tracks and over 38,000 filtered data points spanning approximately 1,500,000 nautical miles. Figure 5 displays the track density incorporated in this study. In Figure 6 we show a histogram of the data coverage with respect to time. The data coverage spans the years 1960 to 1980 with a mean about 1970. Therefore we will define our intermediate wavelength and secular variation fields to epoch 1970. Figure 6 might also serve as an indication of the variation in funding for marine geophysical exploration during the past two decades.

The Technique:

The marine data measure magnetic fields from several sources of internal and external origin. Among the external sources are magnetic storms and the associated DS and DST variations, Auroral and Equatorial electrojets, and ionospheric SQ currents Nagata and Fukushima (1971). Other sources such as magnetospheric boundary currents or micropulsations are either of low amplitude or too high a frequency to affect our study. Internal sources include the core field and shallow crustal magnetic distributions of structural and sea floor spreading type caused by induced or remanent magnetization. Lithospheric scale magnetization distributions are thought to be the sources of the intermediate field. Our objective in filtering the surface field is the removal of the anomaly fields due to all sources except those of lithospheric scale and intermediate wavelength within the interval 3000 to 300 km.

All marine data are first reduced to anomaly form using a Pre-MAGSAT reference field of degree 13 furnished by Dr. R. Langel -MAGSAT Project Scientist. The model includes secular variation estimates also to degree 13. The field model serves as a nominal regional field which can easily be substituted later in the analysis. All variations in the potential field for wavelengths greater than 3000 km. are therefore removed from the observed data if the PreMAGSAT field model is correct.

The total field anomalies of wavelength less than 300 km were filtered from the profiles using a Gaussian filter. The random filtered data points were then processed within 2x2 and 6x6 degree bins. The random orientation of the tracks and the areal nature of the study should overcome the effects of strike aliasing. A true test of the effectiveness of our technique lies in the coherence of the final data set and its comparison to the MAGSAT anomaly field.

We have applied a Gaussian weighted filter to all anomaly profiles to eliminate aliasing from shorter wavelength crustal anomalies. The filter is adapted from McKenzie et al. (1980) and has a spectral cutoff of 300 km. We have filtered point-by-point values of the magnetic anomaly M $(\bar{a}_j, t_j)$, computed Solar Quiet Variation SQ$(\bar{a}_j, t_j)$, and DST estimates DST$(\bar{a}_j, t_j)$.

where $\bar{a}_j$ = The position vector of data point

t_j = the time of data point

The Filtered Magnetic anomaly becomes:

$$(1) \qquad A(\bar{b}_i, t_i) = \sum_j M(\bar{a}_j, t_j)\ \omega_j / \Sigma\ \omega_j$$

where:

$$\bar{b}_i = \sum_j \bar{a}_j \omega_j / \sum_j \omega_j$$

$$\omega_j = \exp(-\chi_j^2 / \sigma^2)$$

$A(\bar{b}_i, t_i)$ = Averaged anomaly value relocated to point b_i

σ = half width of the Gaussian filter

χ_j = is distance to point a_j from the filter centroid.

The spectral response of the Gaussian antialiasisng filter is

$$F(s) = \exp^{(-s^2 \sigma^2 / 4)} \tag{2}$$

where s = scalar wave number.

Figure 7 shows the application of the filter to a given profile. The filter is applied by moving the centroid of the filter at a given increment along the ship's track. All data within a given radius of the centroid is averaged and the resultant value is assigned to the centroid. The filter is incremented at 50 kilometer intervals along track to eliminate aliasing. Note that the filtered value is assigned to a location defined by unit vector $\hat{b}_i$ which is not necessarily coincident with the filter centroid. The Gaussian half width of σ = 100 km was chosen to give a low pass cutoff of approximately 300 km wavelength. Figure 8 displays the spectral response of the Gaussian filter applied to the magnetic data set. Figure 4 also displays the expected amplitudes and wavelengths of various internal and external sources to be measured by a shipboard magnetometer moving at 10-15 knots. Note that DST, DS, SQ, and the crustal sources are of sufficient amplitude to cause considerable error if these field components are not properly filtered.

The marine magnetic data are scalar total field measurements. The anomaly field is obtained by removing a reference field model determined from a spherical harmonic expansion. The assumption is made that the observed field vector is in the direction of the reference field vector. This can be expressed as:

$$(3)\qquad T_{ANO}(x,y) = T_{OBS}(x,y) - T_{REF}(x,y)$$

$$\cong -\hat{t}_{REF}(x,y) \cdot \nabla A_{OBS}(x,y) + \hat{t}_{REF}(x,y) \cdot \nabla A_{REF}(x,y)$$

$$(4)\qquad T_{ANO}(x,y) \cong -\hat{t}_{REF}(x,y) \cdot \nabla A_{ANO}(x,y)$$

$A(x,y)$ = Magnetic scalar potential

$T(x,y)$ = Magnitude of magnetic field vector

$\hat{t}(x,y) = \ell(x,y)\,\hat{i} + m(x,y)\,\hat{j} + n(x,y)\hat{k}$

= unit vector in the direction of the magnetic field vector

$\hat{t}_{OBS} \cong \hat{t}_{REF}$

x,y,z is the coordinate system pointing in the North, East, and down direction respectively with direction cosines l,m,n.

Subscripts: OBS, REF, ANO refer to the observed, reference and anomaly fields respectively.

Taking the two dimensional Fourier Transform of equation 4 we obtain

$$(5)\qquad T_{ANO}(u,v) = (-1)\,[n*s\,A_{ANO}(u,v) + i(\ell*uA_{ANO}(u,v) + m*vA_{ANO}(u,v))]$$

where $s = (u^2+v^2)^{1/2}$

= scalar wave number

* is the convolution operator

Applying the anti-aliasing filter to equation 3 we obtain

$$F_{ANO}(u,v) = T_{ANO}(u,v)\, e^{\frac{-(c^2 s^2)}{4}}$$

Note that if the magnetic field vector is not constant over the study area, the spectrum of the total field anomaly will be convolved or smoothed by the spectrum of the total field direction cosines. The effect is to smear the spectral energy to adjacent wavelengths. For small study areas $\leq 10^6$ km^2, $\hat{t}(x,y)$ can be thought of as constant and our filtering process is a bandpass for $3000 > \lambda > 300$ km. Components of the field are not subject to this convolution effect. Therefore, some intermediate wavelength anomalies may appear in the total field pattern and not in the component field.

Fig. 9 displays the correlation between DS, DST, and Ap (Suguira and Chapman, 1960; Mayaud, 1980). It can be seen that during a large magnetic storm, DS and Ap fall off at approximately equal rates after the main phase of the storm. This may be due to the relationship between substorms and magnetospheric convection. The compilations of Fig. 9 suggest that the contributions of DS can be minimized by excluding data acquired when Ap>30. The remaining ring current field, or DST, can be removed using the estimates of Sugiura (1963) available from the NGSDC, when Ap $\leq$ 30, although the problem of annual variation remains unresolved for the moment.

Figure 10 is a histogram of the occurrence of Ap and DST values for our data set. Less than 5% of the utilized data fall in the Ap >30 range. The effect of the auroral electrojet was avoided by restricting the analysis to latitudes less than 50°N. The equatorial electrojet is also observable in the marine data within the region ±5° from the magnetic equator (Handschumacher, 1976). We have not restricted our data in time or area to avoid the effect of the equatorial electrojet; therefore care must be taken in interpretations near the magnetic equator. The location of the magnetic equator is shown in as a stipled line in Figures 1,2,3,14, and 15.

The diurnal variation or SQ can provide a significant level of variation in the observed anomaly pattern. We have removed SQ utilizing the model of Malin (1973). Figure 11 (a,b,c,d,e) display the SQ model values and the variation in filtered anomaly data with respect to local time. A total of over 38,000 filtered data points were examined and the number of data points for each band is shown in the figures. The diurnal variation is clearly observed in the data set and on the average the Malin model effectively removes this field. Yearly, seasonal and daily variations in SQ were not considered. In performing the averaging it was noticed that the mean of the anomaly data showed a latitudinal dependence. Figure 12 displays the plot of filtered anomaly means and SQ means with respect to latitude. The variation in the mean anomaly is presumably due to errors in the low order terms of the PreMAGSAT regional field.

The ship's field at the sensor is usually less than 5-15 nT, Bullard and Mason (1963), and varies with the ship's heading. Since we are using randomly oriented tracks within a given study area we conclude that the effect is subdued in a large data set. A more serious problem is the effect of poor navigation. Inaccurate navigation results in the calculation of an incorrect reference field which may be several tens of gammas in error. Inspection of individual data sets and the culling of problematic data have reduced the effect of poor quality data in our final compilation.

The filtered values are assembled within 2° x 2° and 6° x 6° bins. The sizes of the bins were chosen to optimize stability of the solutions and spatial resolution. The anomaly values within a given bin are considered to be a function of DST, SQ, secular variation and internal intermediate wavelength sources.

The data within a given bin are approximated by the function

$$A(t) = A_{70} + Vt + DST + SQ$$

where

A = observed anomaly (intermediate wavelength bandpass)

A_{70} = anomaly at epoch 1970

V = secular variation anomaly estimated over the 6°x6° grid

t = time in years since 1970

The application of the DST and SQ estimates significantly improves the regression within most bins. Figure 13 displays a bin centered on 23° North, 171° East. Note the improvement in the distribution of filtered anomaly data with respect to the final linear regression for the corrected bin values. Corrections for SQ tend to reduce the dispersion of filtered anomaly values for a given track line: the DST correction generally improves the regression.

Total Field Secular Variation Anomalies:

The secular variation anomalies (V) were computed as described above by linear regression within 6° x 6° bins. A secular variation anomaly is the error in estimate of secular change of the total field after the removal of the Pre-MAGSAT model ($n \leq 13$). Significant secular variation anomalies in the total field are seen at wavelengths shorter than 5000 km and amplitudes as large as 60 nT/yr west of Hawaii. (Figure 14). These anomalies show strong spatial correlation to the total field anomaly pattern in Figure 15 which is referenced to the pre-MAGSAT field. For example compare the anomalies centered on 30N, 175E and 30N, 165W in Figures 14, 15 and 10. This can easily be observed by superimposing the two maps.

Alldredge et al. (1963), Harrison and Carle (1981) and Carle and Harrison (1982) have shown that the low order terms in the potential field expansions

may contribute to high order terms in the total field. Therefore, the observed secular variation anomalies may reflect errors in the secular variation estimates of the Pre-MAGSAT model for $n \leq 13$. Because of suspected inaccuracies in the original reference field, we have calculated the total observed filtered field and its associated secular variation by adding the field estimates of the original model field to the 2° x 2° and 6° x 6° grid values for total field and secular variation respectively. The anomaly field of Figure 1 was calculated by removal of DGRF 1970 Field (IAGA,1981) to order 10. Figure 2 is a plot of the total observed secular variation, note that the 5000 km wavelength features have disappeared. Some localized short wavelength features do remain in the secular variation field. These features are likely artifacts of strong local anomalies and insufficient data coverage.

Core phenomena might also contribute to secular variation for wavelengths shorter than 3000km. Lowes (1974) notes that the energy in the secular variation appears to fall off less rapidly than the stationary components. This is likely due to the westward drift of the nondipole field components. Therefore, the remaining short wavelength secular variation anomalies may be due to high order core field phenomena. This is interesting in that we may be able to identify some of the intermediate wavelength anomalies as high order core field phenomena.

Finally we must consider that the abrupt truncation of a reference field at a given order will generate an oscillation or ringing (the Gibbs phenomena-Chapman and Bartels, p. 561, 1940; Bracewell, 1971) in the anomaly field for wavelengths longer than the high pass cut-off in this case $\lambda > 3000$ km or $n > 13$. Since the reference field for both Figures 15 and 2 (PreMAGSAT reference field) and the MAGSAT and Pogo fields were truncated at N=13 we would expect similar ringing phenomena. However, the DGRF reference field was truncated at

order and degree 10 therefore the ringing phenomena should differ between these fields. Similarities between the DGRF field and the MAGSAT field should therefore have physical significance since we can eliminate the Gibbs effect as a cause for anomaly correlations. The bandpass for figure 1 after averaging with 2°x2° bins and removal of the degree 10 DGRF is 4000 km to 400 km.

Intermediate Wavelength Total Field Anomalies:

In general a strong correlation exists between the MAGSAT anomaly field Figure 2 and the filtered marine data Figure 1 for the North Pacific. Because the two data sets are derived from independent data sets and different reduction techniques were utilized for each field. The correlation therefore suggests that the techniques applied to each data set are appropriate and that the observed anomalies are not an artifact of processing. Positive anomalies are observed in the satellite and surface fields along the Western Pacific Trench system, (35N, 130E), the Indonesian islands (5N, 130E) and the Central Pacific (25N, 170E). The northwestern Pacific is characterized by high amplitude intermediate wavelength anomalies while the northeastern Pacific exhibits a more subdued pattern. The basement relief in the North Pacific is generally greater in the northwestern Pacific than the northeastern Pacific (Figure 4). The basement relief northwestern Pacific is dominated by lineated seamount chains attributed to hot spot trends or fracture zones (Wuksibm 1965; Morgan, 1973).

A first look at the two intermediate wavelength fields shows that the horizontal gradients of the sea surface data are generally steeper than those of the MAGSAT field. This is expected since the MAGSAT field should be equivalent to the upward continued sea surface data provided no errors exist in either data set. The gradients of the sea surface data generally outline tec-

tonic features such as the western Pacific trench system, the mid Pacific Seamounts, the Hess and Shatsky Rises, the margins of the western Pacific Back Arcs Basins, the Hawaiian Emperor Seamount Chain, and to a lesser extent, the Eastern Pacific Fracture Zones such as the Clipperton, the Clarion and the Mendocino.

Broad anomalies ranging from 1000 km to greater wavelengths are also observed in both fields. The most prominent of these we chose to call the Emperor Anomaly. The Emperor Anomaly at 14 nT., is the largest amplitude anomaly observed in the MAGSAT field over the ocean basins. Our filtered sea surface data set also show this anomaly with a maximum amplitude of 150 nT. focused at the bend of the Emperor Hawaiian seamount chain (Figures 1,2, and 16 to 19) where it intersects the Hess Rise.

The Line Island Chain and Mid-Pacific seamounts separate the broad positive regional anomaly (the Emperor Anomaly) to the north from a generally negative residual field to the south (Figure 1). The anomaly field to the east of the Pacific trench system is generally negative as are the Miocene back arc basins from the Sea of Japan to the Parece Vela Basin. The older Eocene age Philippine Basin displays a relative positive anomaly field (Figures 1, 2 and 23).

The magnetic pattern over the Emperor anomaly of the Western Pacific is observed in both the sea surface data and the satellite field. Figures 16 and 17 display the pattern of the intermediate anomalies with respect to regional bathymetry. The Emperor is bounded on its southern and western margins by a steep negative gradient of 20-40γnT/100km. The southern boundary is strongly correlated to the Mid Pacific Seamount, the Western Boundary also has a seamount lineament and the Shatsky Rise to the Northwest. The Northeastern Boundary is likely the Hess Rise though the maximum of the Emperor Anomaly is

located above the bend in the Emperor Seamount Chain, and the intersection of the Mendocino Fracture Zone.

Though the sharper gradients appear to be due to morphologic features, the broad positive magnetic anomaly of the Emperor Anomaly appears to be related to a zone of high amplitude seafloor spreading type anomalies of Mesozoic age. In Figures 18 and 19 we show the MAGSAT and filtered seasurface fields in relation to the seafloor spreading anomalies. Note that the maximum in the intermediate fields appears to correlate strongly with the maximum amplitude of the seafloor spreading anomalies. The amplitude of the seafloor spreading anomalies may reflect an enhancement in the magnetic mineralogy of the lithospheric plate.This suggests to us that in addition to the magnetic fields of the seamount chains, the Hess and the Shatsky Rises, the region of the Emperor Anomaly may also be associated with a lithosphere of generally hgher susceptibility.

Overlaying the magnetic anomaly maps 1 and 2 over the basin bathymetric shows that linear negative anomalies (40-50 nT negative) are located above the older seamounts of the region (Figures 16 and 17). The seamounts of the Mid Pacific are generally Mid to Late Cretaceous in age and were formed during the Cretaceous normal period south of the magnetic equator (Thiede et al., 1981; Lancelot, 1978; Lancelot and Larson, 1975). The Emperor-Hawaiian chain are Late Cretaceous to Cenozoic in age and were formed near 20°N (Kono, 1980, Harrison et al., 1975). The northward motion of the Pacific has moved them to their present location (Fig. 20).

Figures 16 and 17 show that the aggregate magnetic anomaly pattern of these seamounts is strongly negative at sealevel and weakly negative at the satellite altitudes. A comparison of Figures 16 and 17 shows the strong correlation between the MAGSAT and sea surface fields. The figures also show

that decreased sensitivity of MAGSAT to north-south striking anomalies due to its orbital inclination. Note that the Emperor Seamount anomaly is not observed in MAGSAT while the Emperor Trough anomaly is apparent in both fields.

Figures 16 and 17 show that a positive anomaly exists of the Northwest and Northeast corners of the Emperor anomaly. These appear to be associated with zones of thickened crust named the Shatsky and Hess Rises.

Because most large seafloor features $\lambda > 100$ km are isostatically compensated, we expect that intermediate wavelength topography will be reflected in mantle topography. Wasilewski et al. (1979) have suggested that the Moho forms a lower magnetic boundary within the lithosphere. The work of Wasilewski et al. is based on susceptibility measurements of ultramafics. A direct relationship should therefore exist between seafloor topography and intermediate wavelength anomalies if the hypothesis of Wasilewski et al. (1979) is correct and if oceanic relief is isostatically compensated by lithospheric flexure and crustal thickening (Watts, 1978).

The question of whether the observed fields are due to induced or remanent magnetization is especially interesting since an induced anomaly of the amplitude observed over the Mid Pacific Seamounts would require a substantial root and would support Wasilewski's hypothesis. On the other hand a remanent magnetic source could significantly aid in determining absolute plate rotations from paleomagnetic data. In the region covered by Figures 16,17 we have a good record of plate motion and paleomagnetics as recovered by the Deep Sea Drilling Program and the work of such authors as Harrison et al., 1975; Kono, 1980; Lancelot and Larson, 1975; Lancelot, 1978; Thiede et al., 1981; and Vallier et al., 1981. In order to determine the most important component of magnetization we have formulated two simple models. The first model is a 2-dimensional prism of thickness 4 km and magnetization 3.3 A/m (.0033 emu/cc)

and polarity according to references previously mentioned and listed in the figure caption of Figure 21. The second model is an inductively magnetized prism of thickness 13 km and susceptibility $4x10^{-2}$ SI (.0033 emu/cc). The upper surface of each prism is at 2 km depth. Figure 21 displays the observed anomaly at seasurface and at MAGSAT altitudes. A comparison of the model profiles to the various seamount chains and rises of figures 16 and 17 shows that only for the Marshall-Gilbert, Mid-Pacific and Emperor Seamounts is it possible to distinguish between the two models. The induced anomaly model for the Marshall-Gilbert and Mid Pacific seamounts is much more highly skewed than the observed data. The observed data match the remanent model quite well with the with the minimum of the anomaly directly over the center of mass. The Emperor Seamounts strongly support a remanent model since the induced model requires a positive anomaly where a negative (-10 γ) anomaly is observed in the filtered seasurface field. Unfortunately the North-South lineated anomaly is only slightly recorded in the MAGSAT field. This is presumably due to the directional sensitivity of the MAGSAT field.

Figure 23 displays the filtered sea surface field with respect to the tectonic features of the Western Pacific island arc system. Contours are extended over islands and onto land areas. This is a result of our numerical processing and represents an interpolation or extrapolation of the marine data set. Therefore care must be exercised in interpreting these results. The correlations between the filtered sea surface data and the tectonic structure of the region are surprisingly strong. The similarity of the filtered sea surface field to the MAGSAT field, Figure 24, is generally poor. Some similarity exists along the Japan trench and over the island arcs but the correlation worsens over the back arc system. This may be due to the insensitivity

of the MAGSAT field to north-south lineations which pre-dominate in the region.

One can see a strong correlation in Figure 23 to virtually all known tectonic lineaments. These correlations include local positive anomalies bordering all trenches including the Kuril, Japan, Bonin, Ryukyu, and the Philippine trenches. The only exception being the Mariana trench. A local negative follows the abandoned spreading axis of the Japan Basin, Shikoku and Parece Vela Basins. These basins are likely Miocene to Oligocene in age (Mrozowski and Hayes, 1979; Karig, 1971, 1975; Weissel, 1981; Karig et al., 1975). The older (Eocene) West Philippine Basin (Mrozowzki et al., 1982) shows a local positive anomaly. A weak magnetic gradient is observed over the Central Basin Fault and stronger gradients are located along the boundaries of the Philippine Basin.

Though it is quite obvious that the intermediate wavelength anomalies appear to separate regions of the Western Pacific with differing tectonic histories the causes of the magnetic contrast are not obvious and the application of a single model is fraught with contradictions.

The general correlation of moderate heat flow to the Japan-Parece Vela Basin negative anomaly (Yanagisawa et al., 1982) is contradicted by the older (Eocene) and lower heat flow of the Oki-Daito region. Furthermore, maximum heat flow is observed near the island arc system and not near the axis of the negative magnetic anomaly in the Parece Vela Basin (Anderson et al., 1978). Figure 25a displays a plot of heat flow values with respect to magnetic anomaly. Heat flow values were taken from Anderson et al., 1978. Error bars on the heat flow values are 1 standard deviation. Of course the heat flow values may not accurately reflect the true temperature of the lithosphere due to com-

plications such as local hydrothermal circulation or topographic effects. The correlation is nonetheless weak.

Variations in the chemistry of the oceanic lithosphere may reflect changes in the bulk magnetic mineralogy of the basins. However, Deep Sea Drilling results show that the composition of West Philippine, Shikoku, and Parece-Vela Basin basalts closely resemble the mid-ocean ridge basalts with only a slight increase in alkalinity from the Philippine to the Parece Vela basin (Zakariadze, et al., 1980; Dick, et al., 1980; Marsh, et al., 1980; and Wood et al., 1980). For the moment however, the data are too sparse and the correlation are too subtle to draw any conclusions about the relationship between the magnetic anomaly pattern and the chemical composition of the oceanic lithosphere.

There appears to be moderate correlation between crustal thicknesses and magnetic anomaly amplitude along the West Mariana Ridge and within the Parece-Vela Basin and Japan Sea (Fig. 25b). This would support the alternate hypothesis of Yanagisawa, et al., 1982. No similar correlation is observed within the West Philippine Basin though the seismic data are sparse and very few refraction profiles have measured the depth to Moho along the margine of the West Philippine Basin. We note that ultra basic have been dredged from within the Parece Vela Basin which further suggests a thin crust and shallow Moho (Mrozowski and Hayes, 1979).

There is a strong suggestion that intermediate wavelength anomalies delineate tectonic boundaries. The anomalies are moderately correlated to crustal thickness, and weakly correlated to the measured heat flow though problems in obtaining proper measurement environments may have biased the measured heat flow toward lower values and confused the correlation.

In figure 26 we show that a satisfactory model for the western Pacific can be formulated by varying the lower boundary of the magnetic body in accordance with Moho depth as derived from seismic data (Hayes et al., 1978). Thermal conditions within the plate may further alter this crustal thickness model.

Lineated negative anomalies associated with the Mid Pacific seamounts are observed intersecting the Western Pacific trench system (Figures 1 and 23). It is curious that this lineation of the negative anomalies appears to continue into the back-arc region. It is interesting to speculate that the subduction of the Seamount chain may have left a chemical and structural imprint in the developing back-arc as suggested by Kellerher and McCann (1976).

In the eastern Pacific there is a remarkable correlation between the major fracture zones and the intermediate wavelength anomalies observed in the MAGSAT field (Figure 2) and, to a lesser extent, in the 2°x2° sea surface field (Figure 1). Since there are relatively few tracks in the eastern Pacific to constrain the sea surface field, the MAGSAT field may be more accurate in depicting this correlation, particularly for east-west lineated anomalies. In Figure 27 we show the geophysical data collected by the C.V. Hudson along a track that ran up longitude 150°W, crossing the Clarion, Molokai, Murray and Mendocino fracture zones. (This is the same profile studied by Harrison and Carle, 1981.) Large magnetic anomalies are observed in the observed and smoothed profiles above the fracture zones. More importantly, it is apparent that the fracture zones correspond to changes in the gradients of the 2°x2° sea surface field and in the MAGSAT field as shown in the profiles in the upper part of Figure 27.

We have modeled these anomalies as due simply to a small, .038 SI (.003 emu/cc), susceptibility contrast across the fracture zones (Figure 28). (The

anomalies could also be attributed to a small contrast in the remanent magnetization across the fracture zones.) The fact that the susceptibility (or remanent magnetization) contrasts are maintained over long distances suggests that they may represent long period (30-50 m.y.) variations in the magnetic properties of the crust across the fracture zones. Long term variations in basalt chemistry across fracture zones has been observed in rock samples collected by Challenger drilling in the Atlantic Ocean (Scientific Staff, 1982). The origin of these long term variations are unknown, but may reflect the blocking effect of transform faults on longitudinal flow along the mid-ocean ridge system or as a manifestation of longitudinal cellular convection (Richter and Parsons, 1975).

Conclusion:

We have shown that in regions of relatively high track density, it is possible to recover the intermediate wavelength magnetic anomaly field from marine surveys. Except in cases of north-south lineated anomalies the sea surface anomaly field strongly correlates to the MAGSAT intermediate wavelength field over marine regions therefore verifying the validity of both fields.

In comparing the marine data to the MAGSAT anomaly pattern, the severity of the directional sensitivity has become apparent. Though we cannot quantify this directionality with great precision, a comparison of the Emperor seamount anomaly in the sea surface and the MAGSAT fields suggests that the attenuation of north-south anomalies is approximately a factor of 4. A more careful spectral analysis of the two fields will be required to more accurately quantify this effect.

The observed anomalies over the central correlate strongly with tectonic lineaments of the seafloor. We are able to show that the mid Pacific seamount province and rises are observable in the satellite field and that at least some of these observed anomalies are due to remanent magnetization.

The western Pacific show a strong correlation between tectonic features of the island arc systems and observed positive anomalies. This correlation appears to be due more to variations in crustal thickness than heat flow. The Pacific plate shows many intermediate wavelength magnetic lineaments which may be related to the tectonic history of the Pacific plate. A careful analysis of both the sea surface, and MAGSAT magnetic fields in conjunction with the region's geologic data will undoubtedly reveal more about the sources of these magnetic anomalies and geologic development of the Pacific and other oceanic plates.

Acknowledgements

We wish to acknowledge NASA contract NAS-5-25891 for support of this pilot program and we especially thank Dr. Robert Langel and Harold Oseroff for their patience and support at critical times. Discussions with Drs. Chris Harrison, Bob Parker, Jack Hermance, M. Sugiura, Ron Estes, Mike Mayhew, Gary Karner, Bill Haxby, and Julian Thorne have been especially helpful.

References

Alldredge, L.R., G.D. Van Voorhis, and T.M. Davis, 1963, A magnetic profile around the world, J. Geophys. Res., 68, 3679-3692.

Anderson, R.N., Langseth, M.G., Hayes, D.E., Watanabe, T., Yasui, M., 1978, Heat Flow Thermal Conductivity, Thermal Gradient, in: A Geophysical Atlas of the East and Southeast Asian Seas, ed. Hayes, D.E., SEATAR, pub. Geol. Soc. Am.

Bracewell, R., 1976, The Fourier Transform and its Applications, McGraw Hill Inc., N.Y., 381p.

Bullard, E.C., and R.G. Mason, The magnetic field over the ocean; The Sea, vol. III, M.N. Hill (ed.), Interscience, New York, 1963, 963p.

Carle, H.M. and Harrison, C.G.A., 1982, A problem in representing the Core Magnetic Field of the Earth Using Spherical Harmonics, Geophys. Res. Letts., v. 9, p. 265-268.

Chapman, S. and Bartels, J., 1951, Geomagnetism, vol. II, Oxford University Press, London, pp. 1049.

Chase, T.E., Menard, H.W., and Mammerickx, J., 1971, Topography of the North Pacific, Institute of Marine Resources, Technical Report Series, (Series TR-17).

Cochran, J.R., 1973, Gravity and magnetic investigations in the Guiana Basin, Western Equatorial Atlantic, Geol. Soc. Amer. Bull., vol. 84, 3249-3268.

Dick, H.J.B., Marsh; N.G., Bullen, T.D., 1980, Deep Sea Drilling Project Leg 58 Abyssal Basalts from the Shikoku Basin: Their Petrology and Major-element Geochemistry. in: DeVries Klein, Kobayashi, K., et al., Initial Reports of the Deep Sea Drilling Project, v. 58, Washington (U.S. Government Printing Office), p. 843-872.

Handschumacher, D.W., 1976, Post-Eocene plate tectonics of the eastern Pacific, In: The Geophysics of the Pacific Ocean Basin and Its Margin, G.H. Sutton, M.H. Manghnani, R. Moberly, E.U. McAfee, (eds.), Amer. Geophys. Un. Monogr. 19, 117-202.

Harrison, C.G.A., Jarrard, R.D., Vacquier, V., and Larson, R.L., 1975, Paleomagnetism of Cretaceous Pacific Seamounts, Geophys. J., v. 42, p. 859-882.

Harrison, G.G.A., and Carle, H.M., 1981, Intermediate wavelength magnetic anomalies over ocean basins, J. Geophys. Res., in press.

Hayes, D.E., Houtz, R.E., Jarrard, R.J., Mrozowski, C., Watanabe, T., 1978, Crustal Structure in a Geophysical Atlas of the East and Southeast Asian Seas, ed. Hayes, D.E., SEATAR, Pub. Geol. Soc. of Amer.

IAGA, Working Group 1, 1981, International Geomagnetic Reference Fields: DGRF 1965, DGRF 1970, DGRF 1975 and IGRF 1980, EOS, v. 62, p. 1169.

Karig, D.E., 1971, Structural History of the Mariana Island Arc System, Geol. Soc. Am. Bull., 82, p. 323-344.

Karig, D.E., 1975, Basin Genesis in the Phillipine Sea in: D.E. Karig, J.C. Ingle et al., Initial Reports of the Deep Sea Drilling Project, Vol. XXXL, C.U.S. Government Printing Office, Washington, D.C., p. 857-879.

Kelleher, J. and McCann, W., 1976, Buoyant Zones, Great Earthquakes, and Unstable Boundaries of Subduction, Jour. Geophys. Res., v. 81, p. 4885-4896.

Kono, M., 1980, Paleomagnetism of DSDP Leg 55 Basalts and Implications for the Tectonics of the Pacific Plate, in: Jackson, E.D., Koisumi, I., et al., Initial Reports of the Deep Sea Drilling Project, v. 55, Washington (U.S. Government Printing Office), p. 734-752.

Lancelot, Y., 1978, Relations entre evolution sedifmentaire et tectonique de la Plague Pacifique depuis le Cretace Interier, Societe Geologique de France, Memoire, 134.

Lancelot, Y. and Larson, R.L., 1975, Sedimentary and Tectonic evolution of the northwestern Pacific in: Larson, R.L. and Moberly, R., et al., Initial Reports Deep Sea Drilling Project, 32, Washington (U.S. Government Printing Office, p. 925-939.

Langel, R.A., Phillips, J.D., and Horner, R.J., 1982, Initial Scalar Magnetic Anomaly Map from MAGSAT, Geophys. Res. Letts., v. 9, p. 269-272.

Larson, R.L., and Hilde, T.W.C., 1975, A revised time scale of magnetic reversals for the Early Cretaceous and Late Jurassic, J. Geophys. Res., vol. 80, 2586-2594.

Lowes, F.J., 1974, Spatial Power Spectrum of the Main Geomagnetic Field, and Extrapolation to the Core, Geophys. Jour. R. Astro. Soc., 36, 717-730.

Malin, S.R.C., 1973, Worldwide distribution of geomagnetic tides, Phil. Trans. Roy. Soc. London A., vol. 274, 551-594.

Marsh, N.G., Saunders, A.D., Tarney, J., Dick, H.J.B., 1980, Geochemistry of Basalts from the Shikoku and Daito Basins, Deep Sea Drilling Project, Leg 58, in: deVries, Klein, Kobayashi, K., et al., Initial Reports of the Deep Sea Drilling Project, v. 58: Washington (U.S. Government Printing Office), p. 805-842.

Mayaud, P.N., 1980, Derivation meaning, and use of Geomagnetic indices, A.G.U. Monograph 22, pp. 154.

McKenzie, D., Watts, A., Parson, B., and Roufosse, M., 1980, Planform of mantle convection beneath the Pacific Ocean, Nature, vol. 288, 442-446.

Morgan, W.J., 1973, Plate motions and deep mantle convection, Geol. Soc. Am. Memoir 132, p. 7-22.

Mrozowski, C. and Hayes, D.E., 1979, The evolution of the Parece Vela Basin, Eastern Phillipine Sea, EPSL, 46, p. 49-67.

Mrozowski, C.L., Lewis, S.D., Hayes, D.E., 1982, Complexities in the Tectonic evolution of the West Phillipine Basin, Tectonophysics, v. 82, p. 1-24.

Nagata, T. and Fukushima, N., 1971, Morphology of Magnetic Disturbance in Encyclopedia of Physics, vol. XLIX/3, Springer-Verlag, S. Flugge and K. Rawer, eds., N.Y., 536p.

Nomura, M., 1979, Marine geomagnetic anomalies in the western Pacific region, Bull. Earthquake Res., Inst., 11, 1-42, 1979.

Rabinowitz, P.D. and LaBrecque, J.L., 1979, The Mesozoic South Atlantic Ocean and Evolution of its Continental Margins, J. Geophys. Res., vol. 84, 5973-6002.

Richter, F.M. and Parsons, B., 1975, On the interaction of two scales of convection in the Mantle, Jour. Geophys. Res., v. 80, p. 2529-2541.

Scientific Staff, 1982, Elements traced in the Atlantic, Geotimes 27, 21-22.

Shure, L., and Parker, R.L., 1981, An Alternative explanation for intermediate wavelength magnetic anomalies, Jour. Geophys. Res. (in press).

Sibouet, J.C., and Mascle, J., 1978, Plate Kinematic implications of Atlantic equatorial fracture zone trends, J. Geophys. Res., vol. 83, 3401-3421.

Sugiura, M. and S. Chapman, 1960, The Average Morphology of Geomagnetic Storms with sudden Commencements, Abh. Akad. Wiss, Gottingen, Math-Phys. Kl., Sonderheft Nr. 4, 53pp.

Sugiura, M., 1963, Hourly Values of Equatorial DST for IGY, Goddard Space Flight Center, Greenbelt, Maryland, NASA Rep't X-611-63-131.

Thiede, J., Dean, W., Rea, D., Vallier, T., Adelseck, C., 1981, The Geologic History of the Mid Pacific Mountains in the Central North Pacific Ocean - A Synthesis of Deep Sea Drilling Studies, in: Thiede, J., Vallier, T.L., et al., Initial Reports of the Deep Sea Drilling Project, 62, Washington, D.C., (U.S. Government Printing Office), p. 1073-1120.

Vallier, T.L., Rea, D., Walter, D., Thiede, J., Adelseck, C., 1981, The Geology of the Hess Rise, Central North Pacific Ocean, in: Thiede, J., Vallier, T.L., et al., Initial Reports of the Deep Sea Drilling Project, 62, Washington, D.C., (U.S. Government Printing Office), p. 1031-1072.

Wasilewski, P.J., Thomas, H.H., and Mayhew, M.A., 1979, The MOHO as a Magnetic Boundary, Geophys. Res. Letters, vol. 6, 541-544.

Watts, A.B., 1978, An Analysis of Isostacy in the World's Oceans; 1. Hawaiian-Emperor Seamount Chain, J. Geophys. Res., 83, 5989-6004.

Weissel, J.K., 1981, Magnetic lineations in marginal Basinsof the Western Pacific, Phil. Trans. R. Soc. Lond., A300, p. 223-247.

Wilson, J.T., 1965a, Evidence from ocean islands suggesting movement in the Earth, in: Blackett, P.M.S., Bullard, E., and Runcorn, S.K., eds. A symposium on continental Drift, Roy. Soc. London Phil. Trans. Ser. A, vol. 250, p. 145-167.

Wood, D.A., Joron, J.C., Marsh, N.G., Tarney, J., Treuil, M., 1980, Major- and Trace element variations in Basalts from the North Philippine Sea drilled during Deep Sea Drilling Project Leg 58: A comparative study of Back-Arc-Basin Basalts with Lava series from Japan and mid-ocean ridges. in: deVries, Klein, Kobayashi, K., et al., Initial Reports of the Deep Sea Drilling Project, v. 58: Washington (U.S. Government Printing Office), p. 873.

Yanagisawa, M., Kono, M., Yukutake, T., Fukushima, N., 1982, Preliminary interpretation of Magnetic Anomalies over Japan and its surrounding area, Geophys. Res. Lettrs., v. 9, n. 4, p. 322.

Zakariadze, G.S., Sobolev, A.G., Suschevskaya, N.M., and Dmitriev, L.V., 1980, Petrology of Basalts of Holes 447A, 449, and 450, South Philippine Sea Transect, Deep Sea Drilling Project Leg 59, in: Kroenke, L., Scott, R. et al., Initial Reports of the Deep Sea Drilling Project, Leg 59. Washington (U.S. Government Printing Office), p. 669.

Figure Captions

Figure 1: Filtered seasurface data for the bandpass 4000 km to 400 km as described in the text. The anomaly field is with respect to the DGRF 1970 reference field (IAGA, 1981). The magnetic equator is indicated as a stipled line.

Figure 2: MAGSAT anomaly field from 2°x2° averages. Average altitude is 400 km (Lange et al., 1982).

Figure 3: Map of total field secular variation as derived from the filtered sea surface data. The magnetic equator is indicated by a stipled line.

Figure 4: Bathymetric map of the region from Chase et al., with DSDP drill sites indicated.

Figure 5: Track locations of the data set used in this study.

Figure 6: A histogram of the data set distribution in time. Note that the data set is normally distributed in time about 1970.

Figure 7: Application of the Gaussian filter to a measured magnetic anomaly profile.

Figure 8: Spectral Response of the Gaussian antialiasing filter. Marine crustal sources are assumed to be largely due to seafloor spreading type anomalies of short wavelength and high amplitude.

Figure 9: A correlation between the temporal variations in DS, DST and Ap.

Figure 10: Frequency of DST and Ap values in the marine data set.

Figure 11: Correlation between observed diurnal variation and the SQ model (Malin, 1973) utilized in this study. Data are divided into 10° degree latitudinal bands.

Figure 12: Illustration showing the the PreMAGSAT referenced anomaly field of Figure 15 displays a strong latitudinal variation presumably due to field error. The SQ model is stable throughout the region. Diurnal is the mean anomaly value for each latitudinal band of Fig. 11. SQ is the mean model value for each band.

Figure 13: Application of the regression analysis to data within a 2°x2° km at 22°N and 170° East. Note that corrections for DST and SQ significantly improve the regression. It was found that better stability in the secular variation estimation could be obtained for 6x6 degree bins.

Figure 14: Secular variation anomaly field estimated from 6x6 degree bins referenced to the Premag I field. Note the oscillation in values about the Hawaii suggesting an error in the model.

Figure 15: 6°x6° anomaly field derived from the PreMAGSAT field. Note that the major secular variation anomalies of Figure 14 also appear in the anomaly field, particularly in the region of Hawaii. This indicates the sensitivity of the anomaly field to the selected reference field.

Figure 16: MAGSAT field contoured at a .5nT contour interval. Units are .1nT. Note that there is a slight negative above the Emperor Seamount chain.

Figure 17: Sea surface filtered magnetic anomaly referenced to DGRF 1970 field. Contour interval is 10 nT. Stipled zones are regions above the 4000 meter isobath. Note the strong correlation to the MAGSAT field and Figure 16. Lineated negative anomalies follow the mid-Pacific seamounts, the Marshall-Gilbert and Emperor Sea-

mounts. Positive anomalies overlie the Shatsky and Hess Rises and the Emperor Seamounts.

Figure 18: MAGSAT field referenced to the observed seafloor spreading anomalies (Larson and Hilde, 1975).

Figure 19: Filtered sea surface field with respect to the seafloor spreading anomalies (Larson and Hilde, 1975). Note that the seafloor spreading anomalies of a given age fall off in amplitude as the Emperor anomaly decreases in amplitude. We take this as evidence for a regional variation in crustal lithology emplaced during the creation of this portion of the mid-Pacific in the Jurassic and Early Cretaceous.

Figure 20: Plate motion diagram for DSDP sites as calculated by Lancelot and Larson 1975, and Lancelot (1978).

Figure 21: Model calculations for uniformly magnetized prisms. Two models are considered: (1) Induced prism 200 km wide by 13 km deep. Susceptibility= .04 SI (.0033 emu/cc); (2) Remanent Model= 200 km wide by 4 km deep. Magnetization= 3/3 A/m (.0033 emu/cc). The upper of each model is at 2 km depth. Note that only the remanent and induced models of the Marshall Gilbert/Mid-Pacific and Emperor Seamounts are significantly different.

TABLE

Azimuths, remanent and present field vectors are as follows:

		REMANENT FIELD		PRESENT FIELD	
STRUCTURE	AZIMUTH	I_R	D_R	I_P	D_P
Emperor Smts	90°	-42°	0°	52°	3°
Hawaiian Smts	30°	31°	0°	40°	7°
Mid-Pacific Smts	0°	-31°	0°	31°	9°
Marshall Gilbert Smts	30°	-31°	0°	31°	9°
Shatsky Rise	315°	-10°	0°	42°	-2°
Hess Rise	355°	-10°	0°	48°	8°

Figure 22: Conrad 1007 profile over the Mid-Pacific seamounts showing upward continued field and MAGSAT anomalies. and the negative anomaly associated with the Mid-Pacific Seamounts.

Figure 23: Filtered sea surface anomaly field over the Western Pacific, 45 nT have been added to the observed anomalies. Note the strong correlation between the region's ridge systems and the magnetic field. A negative follows the abandoned back arc systems of the Japan Basin, Shikoku Basin and the Parece Vela Basin. In general a positive anomaly is observed over the abandoned and present island arc systems. The only exception being the Mariana Arc system.

Figure 24: The MAGSAT field above the Western Pacific. The correlation is much poorer than for the Central Pacific. Presumably this is due

to the directional sensitivity of the MAGSAT field. A linear positive is observed above the Arc trench system but the detail of the sea surface field is not observed.

Figure 25a: Plot of observed heat flow averages versus magnetic anomaly compiled for all stations from Anderson et al., 1970. Heat flow values show a broad scatter which can be reduced somewhat by better station election. However, hydro thermal circulation may have seriously biased the values circulation lower heat flow values.

Figure 25b: Correlation between magnetic anomaly value and the depth to basement as taken from the sonobuoy compilations of two correlations are shown one for the Parece Vela Basin-Shikoku-Japan Basin and the other for the West Phillipine Basin. It should be noted that many variables will affect this correlation including body structure and magnetization distributions. The Parece Vela anomalies are generally linear and North-South trending.

Figure 26: An induced model based on the compilations of the western Pacific seismic data may explain the observed intermediate field in terms of variations in the Moho depth. The susceptibility contrast of the body is .063 SI (.005 emu/cc). The subducting plate has little the effect on the anomaly field. The model appears distorted is horizontal scale due to large vertical exaggeration.

Figure 27: (Lower) Magnetic, gravity and bathymetry from the C.V. Hudson along longitude 150°W. (Upper) Filtered 2°x2° sea surface data, upward continued to 400 km (dashed), and the MAGSAT field along the same track as the Hudson profile.

Figure 28: Model for an induced anomaly due to a susceptibility contrast across the eastern Pacific fracture zones. Stippled bodies have a .038 SI (.003 emu/cc) susceptibility, white bodies have a zero susceptibility, azimuth=0°, I_p=50°, D_p=10°, field strength=40000 nT. Filtered profile has a bandpass between 400 and 2000 km.

Appendix A

Tracks and filter parameters used in the calculation of the sea surface intermediate wavelength anomaly field. Parameters and track ID's refer to LDGO program and data libraries.

APPENDIX B

Subroutine FIELDG and the associated Pre-Magsat coefficients used in the generation of the Pre-Magsat reference Field.

32500	V2819M	0	0	0	0	600	50.0	100.0		
32600	V2901M	0	0	0	0	600	50.0	100.0		
32700	V3209M	0	0	0	0	600	50.0	100.0		
32800	V3210M	0	0	0	0	600	50.0	100.0		
32900	V3211M	0	0	0	0	600	50.0	100.0		
33000	V3212M	0	0	0	0	600	50.0	100.0	0.10	0
33100	V3213M	0	0	0	0	600	50.0	100.0		
33200	V3214M	0	0	0	0	600	50.0	100.0	0.10	0
33300	V3305M	0	0	0	0	600	50.0	100.0		
33400	V3308M	0	0	0	0	600	50.0	100.0		
33500	V3309M	0	0	0	0	600	50.0	100.0		
33600	V3310M	0	0	0	0	600	50.0	100.0		
33700	V3311M	0	0	0	0	600	50.0	100.0		
33800	V3312M	0	0	0	0	600	50.0	100.0		
33900	V3313M	0	0	0	0	600	50.0	100.0		
34000	V3401M	0	0	0	0	600	50.0	100.0		
34100	V3402M	0	0	0	0	600	50.0	100.0		
34200	V3403M	0	0	0	0	600	50.0	100.0		
34300	V3404M	0	0	0	0	600	50.0	100.0		
34400	V3405M	0	0	0	0	600	50.0	100.0		
34500	V3503M	0	0	0	0	600	50.0	100.0		
34600	V3504M	0	0	0	0	600	50.0	100.0		
34700	V3505M	0	0	0	0	600	50.0	100.0		
34800	V3506M	0	0	0	0	600	50.0	100.0		
34900	V3603M	0	0	0	0	600	50.0	100.0		
35000	V3604M	0	0	0	0	600	50.0	100.0		
35100	V3605M	0	0	0	0	600	50.0	100.0		
35200	V3606M	0	0	0	0	600	50.0	100.0		
35300	V3607M	0	0	0	0	600	50.0	100.0		
35400	V3608M	0	0	0	0	600	50.0	100.0		
35500	V3609M	0	0	0	0	600	50.0	100.0		
35600	V3610M	0	0	0	0	600	50.0	100.0		
35700	V3611M	0	0	0	0	600	50.0	100.0		
35800	V3612M	0	0	0	0	600	50.0	100.0	0.10	0
35900	V3613M	0	0	0	0	600	50.0	100.0		
36000	V3614M	0	0	0	0	600	50.0	100.0		
36100	V3616M	0	0	0	0	600	50.0	100.0		
36200	VAL16M	0	0	0	0	600	50.0	100.0		
36300	YQ719M	0	0	0	0	600	50.0	100.0		
36400	YQ733M	0	0	0	0	600	50.0	100.0		
36500	ZTES3M	0	0	0	0	600	50.0	100.0	0.10	0
36600	ZTS04M	0	0	0	0	600	50.0	100.0		
36700	ZTS05M	0	0	0	0	600	50.0	100.0	0.10	0
36800	ZTS06M	0	0	0	0	600	50.0	100.0		
36900	ZTS07M	0	0	0	0	600	50.0	100.0		
37000	ZTS2BM	0	0	0	0	600	50.0	100.0	0.10	0
37100	ZTS6BM	0	0	0	0	600	50.0	100.0		

24400	PP29DM	0	0	0	0	600	50.0	100.0		
24500	PP29EM	0	0	0	0	600	50.0	100.0	0.10	0
24600	PP29FM	0	0	0	0	600	50.0	100.0		
24700	PP29GM	0	0	0	0	600	50.0	100.0		
24800	PP301M	0	0	0	0	600	50.0	100.0		
24900	PP304M	0	0	0	0	600	50.0	100.0		
25000	PP623M	0	0	0	0	600	50.0	100.0		
25100	PP71AM	0	0	0	0	600	50.0	100.0		
25200	PP71BM	0	0	0	0	600	50.0	100.0	0.10	0
25300	PP71CM	0	0	0	0	600	50.0	100.0		
25400	PPI5AM	0	0	0	0	600	50.0	100.0	0.10	0
25500	PPI6WM	0	0	0	0	600	50.0	100.0	0.10	0
25600	PPIOFM	0	0	0	0	600	50.0	100.0		
25700	PPIONM	0	0	0	0	600	50.0	100.0	0.10	0
25800	PROA4M	0	0	0	0	600	50.0	100.0		
25900	RFO1 M	0	0	0	0	600	50.0	100.0		
26000	RISE1M	0	0	0	0	600	50.0	100.0		
26100	RREHOM	0	0	0	0	600	50.0	100.0		
26200	SCAN2M	0	0	0	0	600	50.0	100.0		
26300	SCAN3M	0	0	0	0	600	50.0	100.0	0.10	0
26400	SCAN4M	0	0	0	0	600	50.0	100.0		
26500	SCAN5M	0	0	0	0	600	50.0	100.0		
26600	SOT13M	0	0	0	0	600	50.0	100.0		
26700	SSCA4M	0	0	0	0	600	50.0	100.0		
26800	SSHOPM	0	0	0	0	600	50.0	100.0	0.10	0
26900	SSU5DM	0	0	0	0	600	50.0	100.0	0.10	0
27000	SSU6WM	0	0	0	0	600	50.0	100.0	0.10	0
27100	SSU7WM	0	0	0	0	600	50.0	100.0	0.10	0
27200	STX01M	0	0	0	0	600	50.0	100.0		
27300	STX02M	0	0	0	0	600	50.0	100.0		
27400	STX06M	0	0	0	0	600	50.0	100.0		
27500	STX08M	0	0	0	0	600	50.0	100.0		
27600	STX09M	0	0	0	0	600	50.0	100.0		
27700	STX10M	0	0	0	0	600	50.0	100.0		
27800	SV370M	0	0	0	0	600	50.0	100.0		
27900	SV970M	0	0	0	0	600	50.0	100.0		
28000	SWAN1M	0	0	0	0	600	50.0	100.0		
28100	TSD03M	0	0	0	0	600	50.0	100.0	0.10	0
28200	TSD05M	0	0	0	0	600	50.0	100.0		
28300	TSD07M	0	0	0	0	600	50.0	100.0		
28400	TTRA3M	0	0	0	0	600	50.0	100.0		
28500	UM63 M	0	0	0	0	600	50.0	100.0		
28600	UM642M	0	0	0	0	600	50.0	100.0		
28700	UM66AM	0	0	0	0	600	50.0	100.0	0.10	0
28800	UM66DM	0	0	0	0	600	50.0	100.0		
28900	UM67 M	0	0	0	0	600	50.0	100.0		
29000	UM69 M	0	0	0	0	600	50.0	100.0		
29100	V1815M	0	0	0	0	600	50.0	100.0		
29200	V1907M	0	0	0	0	600	50.0	100.0		
29300	V1908M	0	0	0	0	600	50.0	100.0		
29400	V1909M	0	0	0	0	600	50.0	100.0		
29500	V2003M	0	0	0	0	600	50.0	100.0		
29600	V2004M	0	0	0	0	600	50.0	100.0		
29700	V2005M	0	0	0	0	600	50.0	100.0	0.10	0
29800	V2006M	0	0	0	0	600	50.0	100.0	0.10	0
29900	V2007M	0	0	0	0	600	50.0	100.0		
30000	V2008M	0	0	0	0	600	50.0	100.0		
30100	V2104M	0	0	0	0	600	50.0	100.0		
30200	V2105M	0	0	0	0	600	50.0	100.0	0.10	0
30300	V2106M	0	0	0	0	600	50.0	100.0	0.10	0
30400	V2107M	0	0	0	0	600	50.0	100.0		
30500	V2108M	0	0	0	0	600	50.0	100.0		
30600	V2110M	0	0	0	0	600	50.0	100.0	0.10	0
30700	V2112M	0	0	0	0	600	50.0	100.0		
30800	V2113M	0	0	0	0	600	50.0	100.0		
30900	V21A9M	0	0	0	0	600	50.0	100.0		
31000	V21B9M	0	0	0	0	600	50.0	100.0		
31100	V2403M	0	0	0	0	600	50.0	100.0		
31200	V2404M	0	0	0	0	600	50.0	100.0	0.10	0
31300	V2405M	0	0	0	0	600	50.0	100.0	0.10	0
31400	V2406M	0	0	0	0	600	50.0	100.0		
31500	V2407M	0	0	0	0	600	50.0	100.0		
31600	V2809M	0	0	0	0	600	50.0	100.0		
31700	V2810M	0	0	0	0	600	50.0	100.0		
31800	V2811M	0	0	0	0	600	50.0	100.0	0.10	0
31900	V2813M	0	0	0	0	600	50.0	100.0		
32000	V2814M	0	0	0	0	600	50.0	100.0		
32100	V2815M	0	0	0	0	600	50.0	100.0		
32200	V2816M	0	0	0	0	600	50.0	100.0		
32300	V2817M	0	0	0	0	600	50.0	100.0		
32400	V2818M	0	0	0	0	600	50.0	100.0		

16300	IIDO3M	0	0	0	0	600	50.0	100.0	
16400	IIDO4M	0	0	0	0	600	50.0	100.0	
16500	INDP1M	0	0	0	0	600	50.0	100.0	0.10 0
16600	INDP2M	0	0	0	0	600	50.0	100.0	
16700	INDP5M	0	0	0	0	600	50.0	100.0	
16800	JD06 M	0	0	0	0	600	50.0	100.0	
16900	JD08 M	0	0	0	0	600	50.0	100.0	
17000	JD7A M	0	0	0	0	600	50.0	100.0	
17100	JPYN2M	0	0	0	0	600	50.0	100.0	0.10 0
17200	JPYN4M	0	0	0	0	600	50.0	100.0	0.10 0
17300	K7112M	0	0	0	0	600	50.0	100.0	
17400	KH683M	0	0	0	0	600	50.0	100.0	0.10 0
17500	KH84AM	0	0	0	0	600	50.0	100.0	0.10 0
17600	KH84DM	0	0	0	0	600	50.0	100.0	0.10 0
17700	KK711M	0	0	0	0	600	50.0	100.0	0.10 0
17800	KK712M	0	0	0	0	600	50.0	100.0	
17900	KK721M	0	0	0	0	600	50.0	100.0	0.10 0
18000	KK728M	0	0	0	0	600	50.0	100.0	0.10 0
18100	KK72AM	0	0	0	0	600	50.0	100.0	0.10 0
18200	KK730M	0	0	0	0	600	50.0	100.0	0.10 0
18300	KK741M	0	0	0	0	600	50.0	100.0	
18400	KK746M	0	0	0	0	600	50.0	100.0	
18500	KK747M	0	0	0	0	600	50.0	100.0	
18600	KK748M	0	0	0	0	600	50.0	100.0	
18700	KK750M	0	0	0	0	600	50.0	100.0	0.10 0
18800	KK760M	0	0	0	0	600	50.0	100.0	
18900	KK762M	0	0	0	0	600	50.0	100.0	
19000	KK76AM	0	0	0	0	600	50.0	100.0	0.10 0
19100	KK76BM	0	0	0	0	600	50.0	100.0	0.10 0
19200	KK771M	0	0	0	0	600	50.0	100.0	0.10 0
19300	KK772M	0	0	0	0	600	50.0	100.0	
19400	KK773M	0	0	0	0	600	50.0	100.0	
19500	KK774M	0	0	0	0	600	50.0	100.0	
19600	KK775M	0	0	0	0	600	50.0	100.0	0.10 0
19700	KKH01M	0	0	0	0	600	50.0	100.0	
19800	LUS7BM	0	0	0	0	600	50.0	100.0	
19900	MA680M	0	0	0	0	600	50.0	100.0	0.10 0
20000	MA701M	0	0	0	0	600	50.0	100.0	
20100	MA702M	0	0	0	0	600	50.0	100.0	
20200	MA703M	0	0	0	0	600	50.0	100.0	
20300	MA704M	0	0	0	0	600	50.0	100.0	
20400	MA705M	0	0	0	0	600	50.0	100.0	0.10 0
20500	MARA4M	0	0	0	0	600	50.0	100.0	
20600	MMAP M	0	0	0	0	600	50.0	100.0	0.10 0
20700	MNSN1M	0	0	0	0	600	50.0	100.0	
20800	MSNO1M	0	0	0	0	600	50.0	100.0	0.10 0
20900	NNO1AM	0	0	0	0	600	50.0	100.0	
21000	NNO6HM	0	0	0	0	600	50.0	100.0	0.10 0
21100	NOV1AM	0	0	0	0	600	50.0	100.0	
21200	NOV2AM	0	0	0	0	600	50.0	100.0	0.10 0
21300	NOVA1M	0	0	0	0	600	50.0	100.0	0.10 0
21400	NOVA2M	0	0	0	0	600	50.0	100.0	
21500	NOVA3M	0	0	0	0	600	50.0	100.0	
21600	NOVA3M	0	0	0	0	600	50.0	100.0	0.10 0
21700	NOVA9M	0	0	0	0	600	50.0	100.0	
21800	NVA10M	0	0	0	0	600	50.0	100.0	
21900	OWEN5M	0	0	0	0	600	50.0	100.0	0.10 0
22000	P6365M	0	0	0	0	600	50.0	100.0	0.10 0
22100	P6501M	0	0	0	0	600	50.0	100.0	0.10 0
22200	P6829M	0	0	0	0	600	50.0	100.0	0.10 0
22300	P6971M	0	0	0	0	600	50.0	100.0	0.10 0
22400	P7004M	0	0	0	0	600	50.0	100.0	0.10 0
22500	P7008M	0	0	0	0	600	50.0	100.0	
22600	P7103M	0	0	0	0	600	50.0	100.0	
22700	P7201M	0	0	0	0	600	50.0	100.0	0.10 0
22800	P7304M	0	0	0	0	600	50.0	100.0	
22900	PIO64M	0	0	0	0	600	50.0	100.0	0.10 0
23000	PIQ01M	0	0	0	0	600	50.0	100.0	
23100	PP001M	0	0	0	0	600	50.0	100.0	
23200	PP008M	0	0	0	0	600	50.0	100.0	
23300	PP01AM	0	0	0	0	600	50.0	100.0	
23400	PP01BM	0	0	0	0	600	50.0	100.0	
23500	PP25AM	0	0	0	0	600	50.0	100.0	
23600	PP25BM	0	0	0	0	600	50.0	100.0	
23700	PP25CM	0	0	0	0	600	50.0	100.0	
23800	PP25DM	0	0	0	0	600	50.0	100.0	
23900	PP25EM	0	0	0	0	600	50.0	100.0	
24000	PP25FM	0	0	0	0	600	50.0	100.0	
24100	PP25GM	0	0	0	0	600	50.0	100.0	
24200	PP29AM	0	0	0	0	600	50.0	100.0	
24300	PP29CM	0	0	0	0	600	50.0	100.0	0.10 0

8200	C2003M	0	0	0	0	600	50.0	100.0	0.10 0
8300	C2004M	0	0	0	0	600	50.0	100.0	
8400	C2005M	0	0	0	0	600	50.0	100.0	
8500	C2006M	0	0	0	0	600	50.0	100.0	
8600	C2007M	0	0	0	0	600	50.0	100.0	
8700	C2008M	0	0	0	0	600	50.0	100.0	
8800	C2009M	0	0	0	0	600	50.0	100.0	
8900	C2010M	0	0	0	0	600	50.0	100.0	0.10 0
9000	C2011M	0	0	0	0	600	50.0	100.0	
9100	C2202M	0	0	0	0	600	50.0	100.0	
9200	C2204M	0	0	0	0	600	50.0	100.0	
9300	CARR1M	0	0	0	0	600	50.0	100.0	
9400	CARR2M	0	0	0	0	600	50.0	100.0	
9500	CAT01M	0	0	0	0	600	50.0	100.0	
9600	CAT02M	0	0	0	0	600	50.0	100.0	
9700	CCTW2M	0	0	0	0	600	50.0	100.0	
9800	CCTW4M	0	0	0	0	600	50.0	100.0	
9900	CIR02M	0	0	0	0	600	50.0	100.0	0.10 0
10000	CL751M	0	0	0	0	600	50.0	100.0	
10100	CL752M	0	0	0	0	600	50.0	100.0	
10200	CL753M	0	0	0	0	600	50.0	100.0	
10300	CL754M	0	0	0	0	600	50.0	100.0	
10400	CN006M	0	0	0	0	600	50.0	100.0	
10500	CN007M	0	0	0	0	600	50.0	100.0	
10600	CN011M	0	0	0	0	600	50.0	100.0	
10700	DD01AM	0	0	0	0	600	50.0	100.0	
10800	DPSN2M	0	0	0	0	600	50.0	100.0	
10900	EEL30M	0	0	0	0	600	50.0	100.0	0.10 0
11000	EEL31M	0	0	0	0	600	50.0	100.0	0.10 0
11100	ERDC2M	0	0	0	0	600	50.0	100.0	0.10 0
11200	GECSCM	0	0	0	0	600	50.0	100.0	0.10 0
11300	GECSDM	0	0	0	0	600	50.0	100.0	0.10 0
11400	GGEK M	0	0	0	0	600	50.0	100.0	
11500	GGL07M	0	0	0	0	600	50.0	100.0	0.10 0
11600	GGL08M	0	0	0	0	600	50.0	100.0	
11700	GGL09M	0	0	0	0	600	50.0	100.0	
11800	GGL16M	0	0	0	0	600	50.0	100.0	
11900	GGL17M	0	0	0	0	600	50.0	100.0	0.10 0
12000	GGL18M	0	0	0	0	600	50.0	100.0	
12100	GGL19M	0	0	0	0	600	50.0	100.0	0.10 0
12200	GGL20M	0	0	0	0	600	50.0	100.0	0.10 0
12300	GGL22M	0	0	0	0	600	50.0	100.0	
12400	GGL30M	0	0	0	0	600	50.0	100.0	
12500	GGL31M	0	0	0	0	600	50.0	100.0	
12600	GGL32M	0	0	0	0	600	50.0	100.0	0.10 0
12700	GGL33M	0	0	0	0	600	50.0	100.0	
12800	GGL54M	0	0	0	0	600	50.0	100.0	
12900	GGL55M	0	0	0	0	600	50.0	100.0	0.10 0
13000	GGL56M	0	0	0	0	600	50.0	100.0	
13100	GGL57M	0	0	0	0	600	50.0	100.0	
13200	GGL58M	0	0	0	0	600	50.0	100.0	
13300	GGL59M	0	0	0	0	600	50.0	100.0	
13400	GGL60M	0	0	0	0	600	50.0	100.0	
13500	GGL61M	0	0	0	0	600	50.0	100.0	
13600	GGL62M	0	0	0	0	600	50.0	100.0	0.10 0
13700	GGL63M	0	0	0	0	600	50.0	100.0	
13800	GGL64M	0	0	0	0	600	50.0	100.0	
13900	GGL65M	0	0	0	0	600	50.0	100.0	
14000	GGL67M	0	0	0	0	600	50.0	100.0	
14100	GUAY1M	0	0	0	0	600	50.0	100.0	
14200	GUAY2M	0	0	0	0	600	50.0	100.0	
14300	GUAY3M	0	0	0	0	600	50.0	100.0	
14400	HHAKUM	0	0	0	0	600	50.0	100.0	0.10 0
14500	HIL3AM	0	0	0	0	600	50.0	100.0	
14600	HIL3BM	0	0	0	0	600	50.0	100.0	
14700	HT001M	0	0	0	0	600	50.0	100.0	
14800	HT002M	0	0	0	0	600	50.0	100.0	
14900	HT003M	0	0	0	0	600	50.0	100.0	
15000	HT05BM	0	0	0	0	600	50.0	100.0	0.10 0
15100	HT05CM	0	0	0	0	600	50.0	100.0	
15200	HT05DM	0	0	0	0	600	50.0	100.0	
15300	HT669M	0	0	0	0	600	50.0	100.0	
15400	HT869M	0	0	0	0	600	50.0	100.0	
15500	HU140M	0	0	0	0	600	50.0	100.0	
15600	HU145M	0	0	0	0	600	50.0	100.0	
15700	HU150M	0	0	0	0	600	50.0	100.0	
15800	HU155M	0	0	0	0	600	50.0	100.0	
15900	IGU01M	0	0	0	0	600	50.0	100.0	
16000	IGU04M	0	0	0	0	600	50.0	100.0	
16100	IGU05M	0	0	0	0	600	50.0	100.0	
16200	IID02M	0	0	0	0	600	50.0	100.0	

```
 100      100.   -100.     00.0    50.0      0.5 1 210 1 5 0 0 2 0
 200    7TW03M   0    0       0       0   600    50.0   100.0
 300    7TW06M   0    0       0       0   600    50.0   100.0
 400    AAMP1M   0    0       0       0   600    50.0   100.0
 500    AAR07M   0    0       0       0   600    50.0   100.0   0.10 0
 600    ANT02M   0    0       0       0   600    50.0   100.0
 700    ANT04M   0    0       0       0   600    50.0   100.0
 800    ANT05M   0    0       0       0   600    50.0   100.0
 900    ANT11M   0    0       0       0   600    50.0   100.0
1000    ANT13M   0    0       0       0   600    50.0   100.0
1100    ANT14M   0    0       0       0   600    50.0   100.0
1200    ARIS6M   0    0       0       0   600    50.0   100.0
1300    ARS05M   0    0       0       0   600    50.0   100.0   0.10 0
1400    ARS07M   0    0       0       0   600    50.0   100.0   0.10 0
1500    BB12AM   0    0       0       0   600    50.0   100.0
1600    BB12BM   0    0       0       0   600    50.0   100.0   0.10 0
1700    BB12EM   0    0       0       0   600    50.0   100.0
1800    BB12FM   0    0       0       0   600    50.0   100.0
1900    BB12HM   0    0       0       0   600    50.0   100.0
2000    BB21IM   0    0       0       0   600    50.0   100.0
2100    BB21JM   0    0       0       0   600    50.0   100.0   0.10 0
2200    BB31AM   0    0       0       0   600    50.0   100.0
2300    BBN1AM   0    0       0       0   600    50.0   100.0
2400    BBN1BM   0    0       0       0   600    50.0   100.0   0.10 0
2500    BBN5CM   0    0       0       0   600    50.0   100.0
2600    BBNT1M   0    0       0       0   600    50.0   100.0
2700    BNT01M   0    0       0       0   600    50.0   100.0
2800    BNT02M   0    0       0       0   600    50.0   100.0   0.10 0
2900    BNT03M   0    0       0       0   600    50.0   100.0
3000    BNT4AM   0    0       0       0   600    50.0   100.0
3100    BNT4BM   0    0       0       0   600    50.0   100.0   0.10 0
3200    BNT5AM   0    0       0       0   600    50.0   100.0   0.10 0
3300    BNT5BM   0    0       0       0   600    50.0   100.0
3400    BNT7AM   0    0       0       0   600    50.0   100.0
3500    C0806M   0    0       0       0   600    50.0   100.0
3600    C0909M   0    0       0       0   600    50.0   100.0
3700    C1004M   0    0       0       0   600    50.0   100.0
3800    C1005M   0    0       0       0   600    50.0   100.0
3900    C1006M   0    0       0       0   600    50.0   100.0
4000    C1007M   0    0       0       0   600    50.0   100.0   0.10 0
4100    C1008M   0    0       0       0   600    50.0   100.0   0.10 0
4200    C1010M   0    0       0       0   600    50.0   100.0   0.10 0
4300    C1011M   0    0       0       0   600    50.0   100.0
4400    C1107M   0    0       0       0   600    50.0   100.0
4500    C1108M   0    0       0       0   600    50.0   100.0   0.10 0
4600    C1109M   0    0       0       0   600    50.0   100.0   0.10 0
4700    C1110M   0    0       0       0   600    50.0   100.0
4800    C1111M   0    0       0       0   600    50.0   100.0
4900    C1202M   0    0       0       0   600    50.0   100.0
5000    C1203M   0    0       0       0   600    50.0   100.0
5100    C1204M   0    0       0       0   600    50.0   100.0   0.10 0.
5200    C1205M   0    0       0       0   600    50.0   100.0   0.10 0
5300    C1206M   0    0       0       0   600    50.0   100.0
5400    C1207M   0    0       0       0   600    50.0   100.0   0.10 0
5500    C1208M   0    0       0       0   600    50.0   100.0   0.10 0
5600    C1209M   0    0       0       0   600    50.0   100.0
5700    C1210M   0    0       0       0   600    50.0   100.0
5800    C1211M   0    0       0       0   600    50.0   100.0   0.10 0
5900    C1216M   0    0       0       0   600    50.0   100.0
6000    C1217M   0    0       0       0   600    50.0   100.0
6100    C1218M   0    0       0       0   600    50.0   100.0
6200    C1219M   0    0       0       0   600    50.0   100.0   0.10 0
6300    C1220M   0    0       0       0   600    50.0   100.0   0.10 0
6400    C1301M   0    0       0       0   600    50.0   100.0
6500    C1302M   0    0       0       0   600    50.0   100.0
6600    C1303M   0    0       0       0   600    50.0   100.0
6700    C1304M   0    0       0       0   600    50.0   100.0   0.10 0
6800    C1305M   0    0       0       0   600    50.0   100.0
6900    C1307M   0    0       0       0   600    50.0   100.0
7000    C1308M   0    0       0       0   600    50.0   100.0
7100    C1402M   0    0       0       0   600    50.0   100.0
7200    C1403M   0    0       0       0   600    50.0   100.0
7300    C1404M   0    0       0       0   600    50.0   100.0
7400    C1405M   0    0       0       0   600    50.0   100.0   0.10 0
7500    C1407M   0    0       0       0   600    50.0   100.0
7600    C1501M   0    0       0       0   600    50.0   100.0
7700    C1709M   0    0       0       0   600    50.0   100.0
7800    C1710M   0    0       0       0   600    50.0   100.0
7900    C1711M   0    0       0       0   600    50.0   100.0
8000    C1712M   0    0       0       0   600    50.0   100.0
8100    C2002M   0    0       0       0   600    50.0   100.0
```

```
C*********************************************************************
      SUBROUTINE FIELDG (DLAT,DLONG,ALT,TM,NMX,L,X,Y,Z,F)
C         MODIFIED JULY 22,1981
C        FOR DOCUMENTATION OF THIS SUBROUTINE AND SUBROUTINE FIELD SEE :
C             NATIONAL SPACE SCIENCE DATA CENTER'S PUBLICATION
C                  COMPUTATION OF THE MAIN GEOMAGNETIC FIELD FROM
C                  SPHERICAL HARMONIC EXPANSIONS
C                   DATA USERS' NOTE,NSSDC 68-11, MAY 1968
C                   GODDARD SPACE FLIGHT CENTER,GREENBELT,MD.
        EQUIVALENCE (SHMIT(1,1),TG(1,1))
        COMMON NDPY(3),LPYR(4),JBSYR
      COMMON /COEFFS/TG(18,18),G(18,18),GT(18,18),GTT(18,18),TLAST
        1,TZERO
      COMMON /FLDCOM/ST,CT,SPH,CPH,R,NMAX,BT,BP,BR,B
        DIMENSION AID(11),SHMIT(18,18)
      DATA A/0./
      A=6378.16
      FLAT=1.-1./298.25
      A2=A**2
      A4=A**4
      B2=(A*FLAT)**2
      A2B2=A2*(1.-FLAT**2)
      A4B4=A4*(1.-FLAT**4)
C*******IF L.LE.0 DON'T READ COEFFICIENTS FILE
      IF (L) 1,1,2
C*******IF DATE IS THE SAME AS LAST DON'T UPDATE COEFFICIENTS
1     IF (TM-TLAST) 17,19,17
C*******READ FIELD COEFFICIENTS
2     READ (3,3) J,K,TZERO,(AID(I),I=1,11)
3     FORMAT (2I1,1X,F6.1,10A6,A3)
      L=0
4     FORMAT (2I3,5X6HEPOCH=,F7.1,5X10A6,A3)
      MAXN=0
      TEMP=0.
5     READ (3,6,END=74) N,M,GNM,HNM,GTNM,HTNM,GTTNM,HTTNM
        WRITE(5,6)N,M,GNM,HNM,GTNM,HTNM,GTTNM,HTTNM
6     FORMAT (2I3,6F11.4)
      IF (N.LE.0) GOTO74
      MAXN=(MAXO(N,MAXN))
      G(N,M)=GNM
      GT(N,M)=GTNM
      GTT(N,M)=GTTNM
      IF (M.EQ.1) GOTO5
      G(M-1,N)=HNM
      GT(M-1,N)=HTNM
      GTT(M-1,N)=HTTNM
      GO TO 5
 74     CONTINUE
C*********WRITE COEFFICIENTS FOR DEBUGGING PURPOSES
D7      WRITE (5,8)
D8      FORMAT (6H0 N  M,6X1HG,10X1HH,9X2HGT,9X2HHT,8X3HGTT8X3HHTT//)
D        WRITE(5,239)MAXN
D239    FORMAT(I10)
D     DO 12 N=2,MAXN
D     DO 12 M=1,N
D     MI=M-1
D       IF(M.EQ.1)GO TO 10
D     WRITE (5,9) N,M,G(N,M),G(MI,N),GT(N,M),GT(MI,N),GTT(N,M),GTT(MI,N)
D9     FORMAT (2I3,6F11.4)
D       GO TO 12
D10    WRITE (5,11) N,M,G(N,M),GT(N,M),GTT(N,M)
D11    FORMAT (2I3,F11.4,11X,F11.4,11XF11.4)
D12     CONTINUE
C*******K.NE.0 IF COEFFICIENTS ARE GAUSS QUASINORMALIZED
C*******K.EQ.0 IF COEFFICIENTS ARE SCHMIDT QUASINORMALIZED
14    IF (K.NE.0) GOTO17
      SHMIT(1,1)=-1.
      DO 15 N=2,MAXN
      SHMIT(N,1)=SHMIT(N-1,1)*FLOAT(2*N-3)/FLOAT(N-1)
      SHMIT(1,N)=0.
      JJ=2
      DO 15 M=2,N
      SHMIT(N,M)=SHMIT(N,M-1)*SQRT(FLOAT((N-M+1)*JJ)/FLOAT(N+M-2))
      SHMIT(M-1,N)=SHMIT(N,M)
15    JJ=1
      DO 16 N=2,MAXN
      DO 16 M=1,N
      G(N,M)=G(N,M)*SHMIT(N,M)
      GT(N,M)=GT(N,M)*SHMIT(N,M)
      GTT(N,M)=GTT(N,M)*SHMIT(N,M)
      IF (M.EQ.1) GOTO16
```

```
      G(M-1,N)=G(M-1,N)*SHMIT(M-1,N)
      GT(M-1,N)=GT(M-1,N)*SHMIT(M-1,N)
      GTT(M-1,N)=GTT(M-1,N)*SHMIT(M-1,N)
16    CONTINUE
17    T=TM-TZERO
      DO 18 N=1,MAXN
      DO 18 M=1,N
      TG(N,M)=G(N,M)+T*(GT(N,M)+GTT(N,M)*T)
C**********BE CAREFUL THAT SECULAR ACCELERATION TERMS ARE DEFINED AS
C********** A*T/2.
      IF (M.EQ.1) GOTO18
      TG(M-1,N)=G(M-1,N)+T*(GT(M-1,N)+GTT(M-1,N)*T)
18    CONTINUE
      TLAST=TM
19    DLATR=DLAT/57.2957795
      SINLA=SIN(DLATR)
      RLONG=DLONG/57.2957795
      CPH=COS(RLONG)
      SPH=SIN(RLONG)
      IF (J.EQ.0) GOTO20
C******IF J.NE.0 OUTPUT IS IN GEOCENTRIC COORDINATES
      R=ALT+6371.0
      CT=SINLA
      GO TO 21
C*****CALCULATE GEODETIC CONSTANTS
20    SINLA2=SINLA**2
      COSLA2=1.-SINLA2
      DEN2=A2-A2B2*SINLA2
      DEN=SQRT(DEN2)
      FAC=(((ALT*DEN)+A2)/((ALT*DEN)+B2))**2
      CT=SINLA/SQRT(FAC*COSLA2+SINLA2)
      R=SQRT(ALT*(ALT+2.*DEN)+(A4-A4B4*SINLA2)/DEN2)
21    ST=SQRT(1.-CT**2)
C******EVALUATE SPHERICAL HARMONIC TO ORDER AND DEGREE NMAX (NOTE:
C******NMAX IS N+1 OF MATH EXPRESSION I.E.  NMAX 14=DEGREE 13 TO
C*******SATISFY THE COMPUTER DO LOOPS
      NMAX=MINO(NMX,MAXN)
C*******EVALUATE SPHERICAL HARMONICS
      CALL FIELD
      Y=BP
      F=B
      IF (J) 22,23,22
22    X=-BT
      Z=-BR
      RETURN
C     TRANSFORMS FIELD TO GEODETIC DIRECTIONS
23    SIND=SINLA*ST-SQRT(COSLA2)*CT
      COSD=SQRT(1.0-SIND**2)
      X=-BT*COSD-BR*SIND
      Z=BT*SIND-BR*COSD
D       WRITE(5,1212)DLAT,DLONG,TM,X,Y,Z,F
 1212   FORMAT(7F8.1)
      RETURN
      END
      SUBROUTINE FIELD
        COMMON NDPY(3),LPYR(4),JBSYR
        COMMON/COEFFS/G(18,18),GX(18,18),GT(18,18),GTT(18,18),TLAST
        1,TZERO
      COMMON/FLDCOM/ST,CT,SPH,CPH,R,NMAX,BT,BP,BR,B
      DIMENSION P(18,18),DP(18,18),CONST(18,18),SP(18),CP(18),FN(18),
     1FM(18)
      IF (P(1,1).EQ.1.0) GO TO 3
1     P(1,1)=1.
      DP(1,1)=0.
      SP(1)=0.
      CP(1)=1.
      DO 2 N=2,18
      FN(N)=N
      DO 2 M=1,N
      FM(M)=M-1
2     CONST(N,M)=FLOAT((N-2)**2-(M-1)**2)/FLOAT((2*N-3)*(2*N-5))
3     SP(2)=SPH
      CP(2)=CPH
      DO 4 M=3,NMAX
      SP(M)=SP(2)*CP(M-1)+CP(2)*SP(M-1)
4     CP(M)=CP(2)*CP(M-1)-SP(2)*SP(M-1)
      AOR=6371.2/R
      AR=AOR**2
      BT=0.
      BP=0.
      BR=0.
```

```
      DO 8 N=2,NMAX
      AR=AOR*AR
      DO 8 M=1,N
      IF (N-M) 6,5,6
5     P(N,N)=ST*P(N-1,N-1)
      DP(N,N)=ST*DP(N-1,N-1)+CT*P(N-1,N-1)
      GO TO 7
6     P(N,M)=CT*P(N-1,M)-CONST(N,M)*P(N-2,M)
      DP(N,M)=CT*DP(N-1,M)-ST*P(N-1,M)-CONST(N,M)*DP(N-2,M)
7     PAR=P(N,M)*AR
      IF (M.EQ.1) GO TO 9
      TEMP=G(N,M)*CP(M)+G(M-1,N)*SP(M)
      BP=BP-(G(N,M)*SP(M)-G(M-1,N)*CP(M))*FM(M)*PAR
      GO TO 10
9     TEMP=G(N,M)*CP(M)
      BP=BP-(G(N,M)*SP(M))*FM(M)*PAR
10    BT=BT+TEMP*DP(N,M)*AR
8     BR=BR-TEMP*FN(N)*PAR
      BP=BP/ST
      B=SQRT(BT*BT+BP*BP+BR*BR)
      RETURN
      END
```

```
00 1960.0    GSFC PREMAG1 (14,14) EPOCH=1960.0    A=6341.2    F=298.25
  2  1-30452.1000      0.0        23.7520      0.0          0.0          0.0
  2  2 -2171.5000   5834.5400     11.0912     -9.3881       0.0          0.0
  3  1 -1543.5900      0.0       -23.6237      0.0          0.0          0.0
  3  2  2992.9800  -1981.6500      1.0427     -6.0416       0.0          0.0
  3  3  1585.5100    212.7270      1.6995    -18.3544       0.0          0.0
  4  1  1304.7700      0.0        -2.7163      0.0          0.0          0.0
  4  2 -1988.2900   -438.3460    -10.9212      7.0997       0.0          0.0
  4  3  1295.6200    233.0490     -2.0714      1.5963       0.0          0.0
  4  4   865.6740   -174.5270     -2.2603     -4.3583       0.0          0.0
  5  1   954.2870      0.0        -1.1912      0.0          0.0          0.0
  5  2   812.0310    136.1850     -1.4004      3.3772       0.0          0.0
  5  3   500.9100   -278.7620     -3.6766      1.0738       0.0          0.0
  5  4  -378.0990     11.1128     -1.3809      1.1670       0.0          0.0
  5  5   275.2710   -241.4930     -4.5806     -2.8827       0.0          0.0
  6  1  -222.3320      0.0         1.0018      0.0          0.0          0.0
  6  2   359.8670     12.6742      0.0446      0.9806       0.0          0.0
  6  3   249.9480    114.5650      1.3429      2.4208       0.0          0.0
  6  4   -19.2541   -101.3940     -2.0854     -3.0060       0.0          0.0
  6  5  -155.0020   -106.6370     -0.7501      2.0907       0.0          0.0
  6  6   -70.9389     51.8397      0.5085      1.6224       0.0          0.0
  7  1    41.0175      0.0         0.3672      0.0          0.0          0.0
  7  2    58.7832    -10.2904      0.4776     -0.2323       0.0          0.0
  7  3    -2.4079    106.0420      1.7966     -0.3307       0.0          0.0
  7  4  -238.5830     62.2257      2.2707      1.1895       0.0          0.0
  7  5    -6.5753    -37.8430      0.8038     -0.4007       0.0          0.0
  7  6    -6.3706    -19.0708      1.5199      0.3546       0.0          0.0
  7  7   -88.8067     -2.0597     -1.6451      3.5104       0.0          0.0
  8  1    72.4081      0.0        -0.3000      0.0          0.0          0.0
  8  2   -53.1911    -55.6066     -0.0144     -1.3414       0.0          0.0
  8  3    -1.4095    -26.8871      0.0046     -0.0325       0.0          0.0
  8  4     8.9282    -10.7983      0.6028      0.1696       0.0          0.0
  8  5   -35.3203      3.1835      1.4086      0.4245       0.0          0.0
  8  6    -1.1347     31.7398      0.2407     -0.2976       0.0          0.0
  8  7    14.9015     -2.5129     -1.1074     -1.6690       0.0          0.0
  8  8   -34.4038    -53.3257      2.5005      0.4367       0.0          0.0
  9  1    11.0202      0.0         0.1968      0.0          0.0          0.0
  9  2     3.0248      7.3400      0.2916      0.1595       0.0          0.0
  9  3    -6.8150    -13.5012      0.5765     -0.1146       0.0          0.0
  9  4   -18.1829      7.3109      0.8121     -0.2587       0.0          0.0
  9  5    -1.5881    -13.6024     -0.2094     -0.3901       0.0          0.0
  9  6    13.4636     14.5928     -1.1174     -0.4462       0.0          0.0
  9  7   -14.7581     14.7982      1.2860     -0.3884       0.0          0.0
  9  8     8.8653     -6.2293     -0.0513      0.0010       0.0          0.0
  9  9    27.6659     10.5759     -3.1399     -1.4777       0.0          0.0
 10  1     8.6246      0.0        -0.0205      0.0          0.0          0.0
 10  2     8.1694    -22.3338      0.0038     -0.1244       0.0          0.0
 10  3     6.3429     13.8975     -0.4359      0.1891       0.0          0.0
 10  4    -9.8288      1.8808     -0.2164      0.4797       0.0          0.0
 10  5    14.9175     -0.1417     -0.5291     -0.1326       0.0          0.0
 10  6     6.2342     -9.4786     -0.9419      0.1777       0.0          0.0
 10  7    -1.8658     -6.0963      0.5379      1.3047       0.0          0.0
 10  8     9.3898     22.7767     -0.3582     -0.2832       0.0          0.0
 10  9     0.4242      6.4458      0.6342     -0.3878       0.0          0.0
 10 10   -14.3130    -34.5974      0.5547      3.7125       0.0          0.0
 11  1    -2.2299      0.0         0.0041      0.0          0.0          0.0
 11  2    -4.6213      5.0375      0.2202     -0.3744       0.0          0.0
 11  3     4.4385      3.1052     -0.1674     -0.2772       0.0          0.0
 11  4     1.2793      1.5856     -0.6292     -0.0597       0.0          0.0
 11  5    -1.3098      7.6086     -0.1139     -0.1997       0.0          0.0
 11  6    -0.9974     -4.1284      0.9014     -0.2655       0.0          0.0
 11  7    15.3318      2.5530     -1.1565     -0.0234       0.0          0.0
 11  8    -3.2109      5.7351      0.4386     -0.6391       0.0          0.0
 11  9    -2.9023    -11.6722      0.7084      1.2878       0.0          0.0
 11 10     4.7863      7.9897     -0.4505     -1.1128       0.0          0.0
 11 11   -16.1481      9.4772      2.3741     -0.5027       0.0          0.0
 12  1     3.4064      0.0        -0.1746      0.0          0.0          0.0
 12  2    -0.2052      1.6326      0.0193      0.1070       0.0          0.0
 12  3    -2.7248      2.8587      0.0268      0.0046       0.0          0.0
 12  4     3.2204      2.4821      0.0571     -0.4512       0.0          0.0
 12  5    -6.1385     -5.8210      0.5920      0.2162       0.0          0.0
 12  6    -0.0226      3.9979      0.1297     -0.1661       0.0          0.0
 12  7    -2.4953      7.2421      0.0235     -0.7093       0.0          0.0
 12  8    -1.6846      3.0473      0.3127     -0.8235       0.0          0.0
 12  9     4.1828     -9.0639     -0.3453      0.5943       0.0          0.0
 12 10    -3.3899     11.5000      0.4515     -1.1986       0.0          0.0
 12 11    16.4696      0.6636     -1.3535      0.2108       0.0          0.0
 12 12     2.4070     15.7471     -1.1228     -1.2665       0.0          0.0
 13  1    -1.3164      0.0         0.0168      0.0          0.0          0.0
 13  2     4.5724     -0.5249     -0.5249      0.0992       0.0          0.0
 13  3    -3.2595      0.0726      0.2161      0.0588       0.0          0.0
```

13	4	-3.2440	-2.0017	0.3430	0.4584	0.0	0.0
13	5	0.3327	-1.8109	-0.0092	0.1356	0.0	0.0
13	6	4.2482	-2.9342	-0.4745	0.4160	0.0	0.0
13	7	-3.1661	-0.4072	0.2680	0.0563	0.0	0.0
13	8	-2.3015	-8.1845	0.1199	0.7403	0.0	0.0
13	9	1.2904	3.9351	-0.1962	-0.2361	0.0	0.0
13	10	0.1247	-1.6214	0.0504	0.2505	0.0	0.0
13	11	4.5984	-4.9478	-0.6032	0.0617	0.0	0.0
13	12	-13.6485	5.7759	0.9665	-0.4208	0.0	0.0
13	13	14.8286	-9.6344	-0.7025	1.3801	0.0	0.0
14	1	1.1168	0.0	0.0424	0.0	0.0	0.0
14	2	-4.4189	1.4957	0.3421	-0.2609	0.0	0.0
14	3	0.2580	0.0051	0.0613	-0.0674	0.0	0.0
14	4	-1.0441	1.4617	0.0138	-0.0698	0.0	0.0
14	5	1.6748	2.6017	-0.1056	-0.2274	0.0	0.0
14	6	-0.0434	2.5333	0.0631	-0.3158	0.0	0.0
14	7	-0.7599	-4.4447	0.1390	0.2612	0.0	0.0
14	8	0.9916	2.3089	-0.1912	0.0511	0.0	0.0
14	9	-0.4356	4.6922	0.0718	-0.3200	0.0	0.0
14	10	-2.7842	-3.6018	0.0620	0.2890	0.0	0.0
14	11	2.5412	-3.2590	-0.2916	0.1212	0.0	0.0
14	12	-2.6202	-3.1924	0.5657	0.2018	0.0	0.0
14	13	8.9108	8.0881	-0.8535	-0.6448	0.0	0.0
14	14	-25.6531	8.0251	2.1563	-0.7430	0.0	0.0

FILTERED SEA SURFACE FIELD

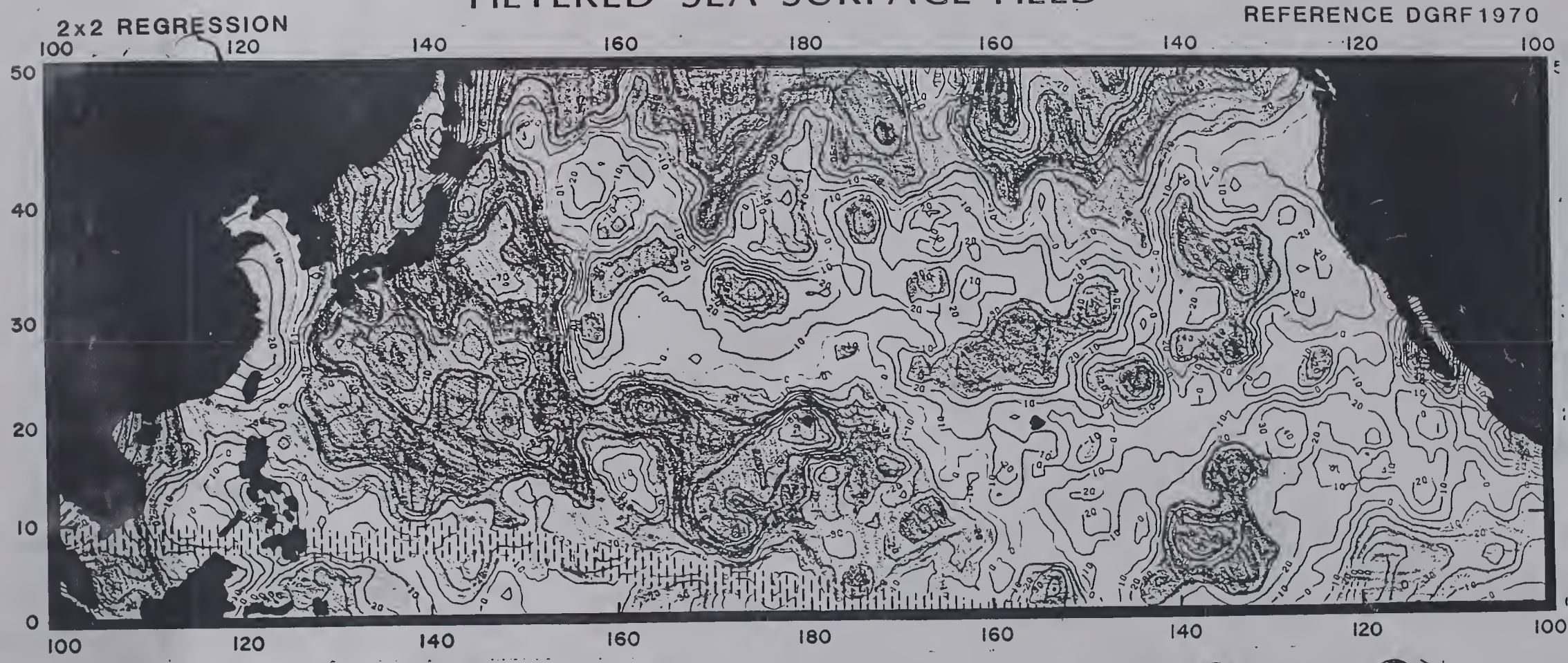

Figure 1

MAGSAT ANOMALY

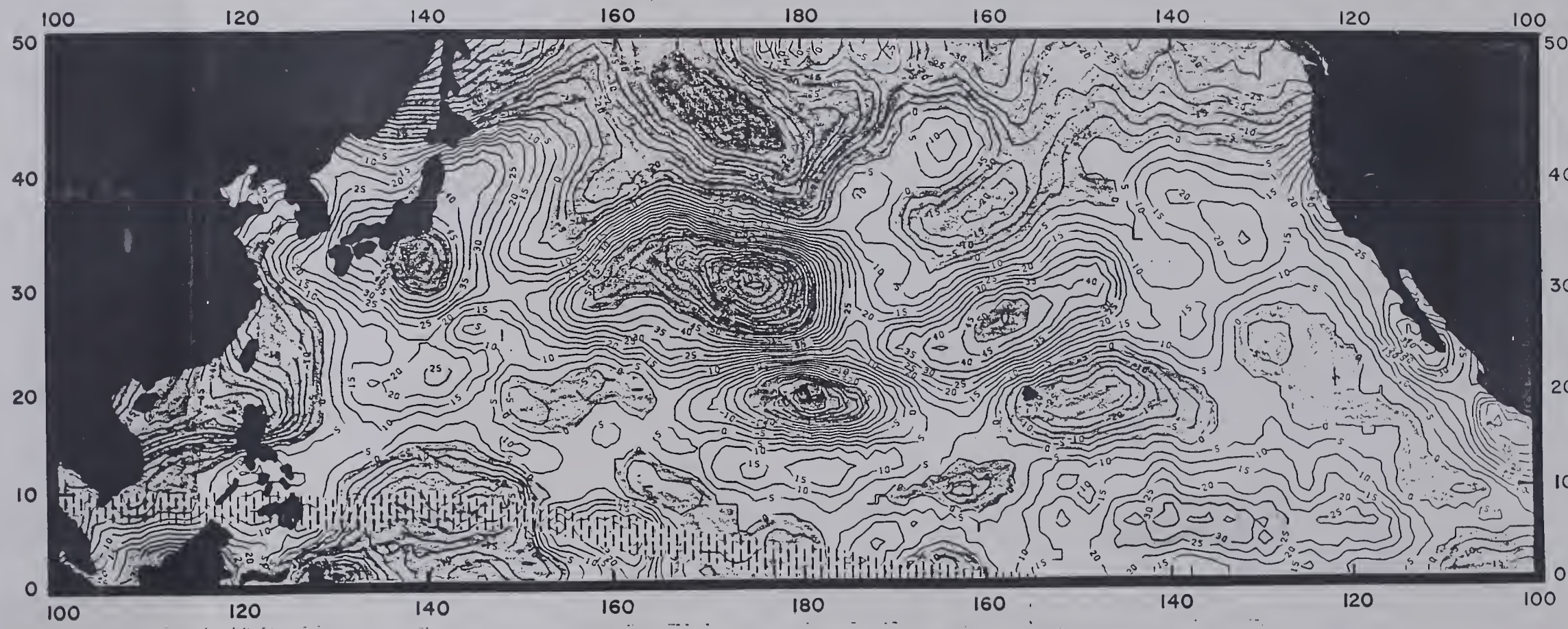

Figure 2

TOTAL SECULAR VARIATION

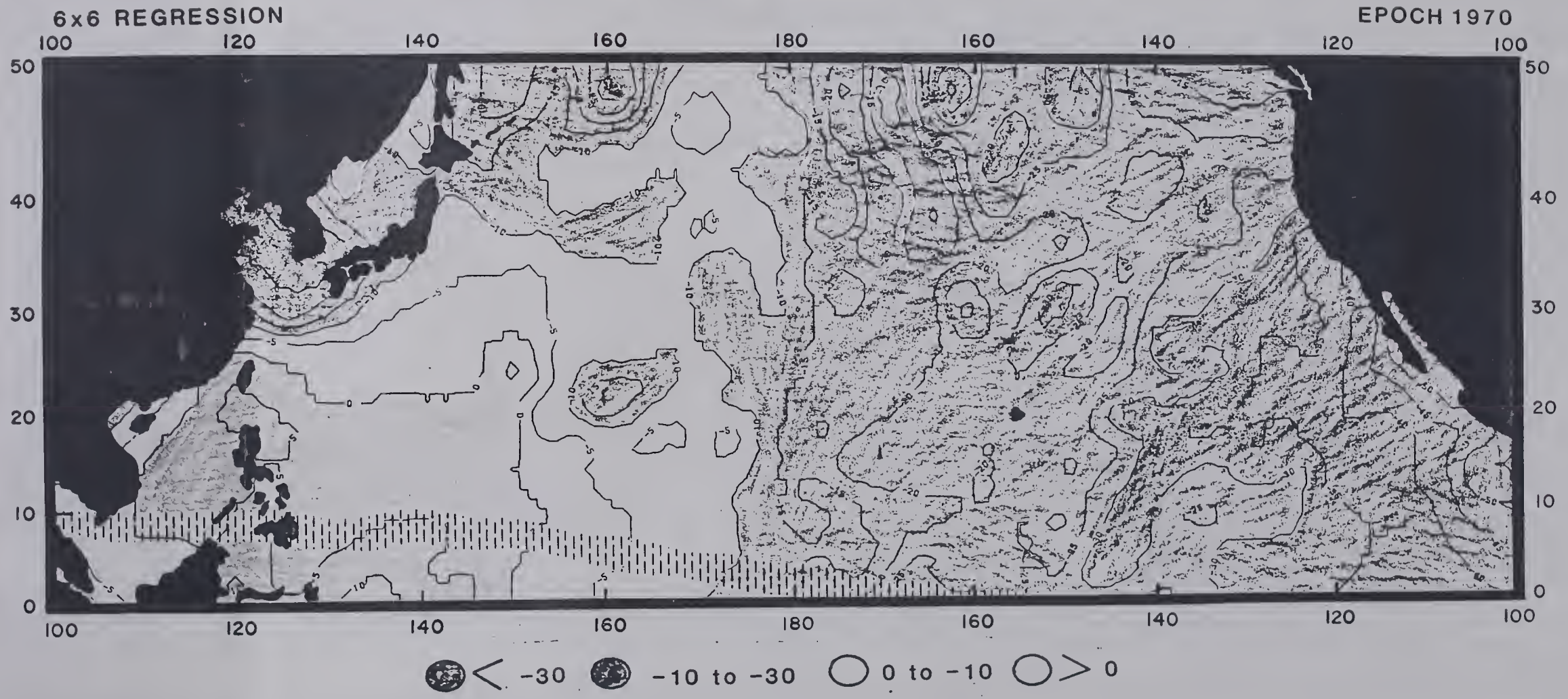

Figure 3

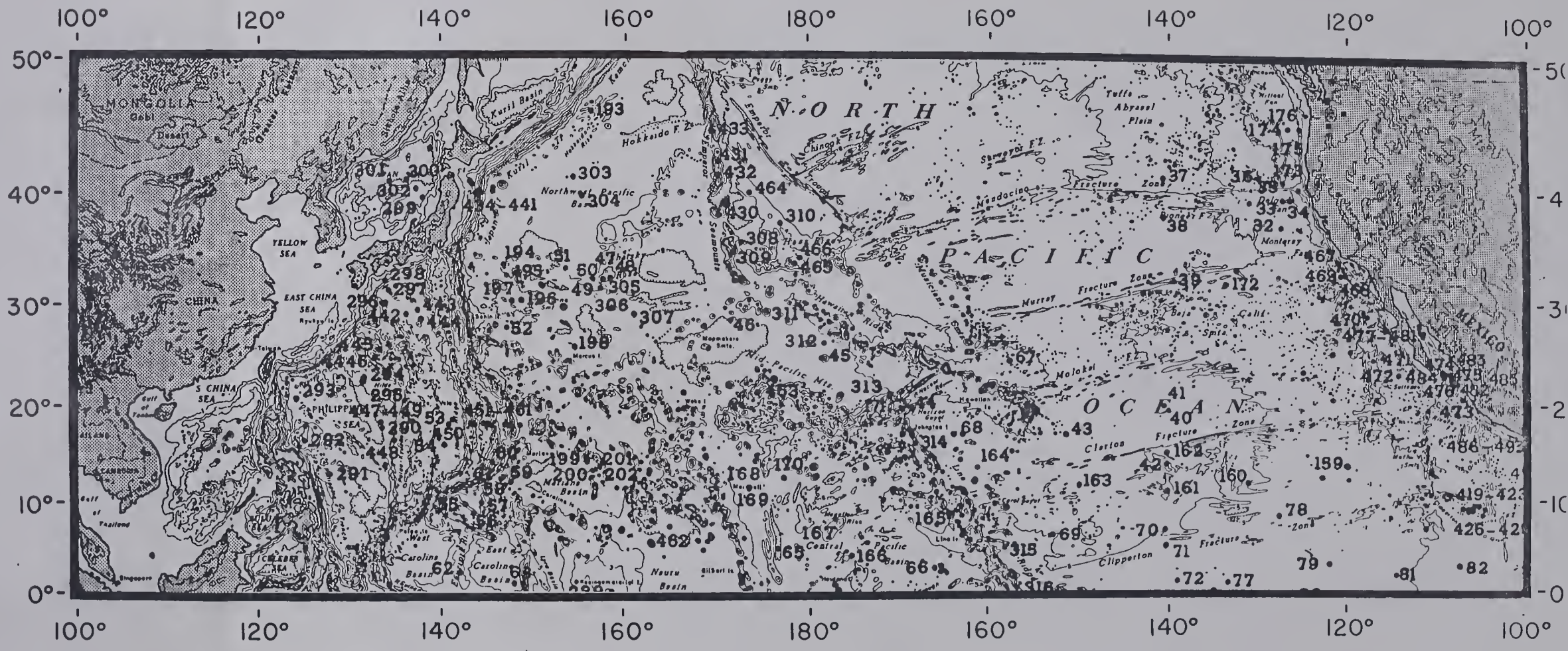
100°
120°
140°
160°
180°
160°
140°
120°
100°
50°
40°
30°
20°
10°
0°
N O R T H
P A C I F I C
O C E A N
MONGOLIA
Gobi
Desert
YELLOW SEA
CHINA
EAST CHINA SEA
S CHINA SEA
PHILIPPINE SEA
CELEBES SEA
Kuril Basin
Kuril I.
Hokkaido F.Z.
Northwest Pacific Basin
Japan
Emperor Seamounts
Hawaiian Ridge
Mid-Pacific Mts.
Moanakea Seamt.
Marcus I.
Wake I.
Marianas Basin
West Caroline Basin
East Caroline Basin
Nauru Basin
Gilbert Is.
Central Pacific Basin
Line Is.
Tuscarora F.Z.
Murray Fracture Zone
Molokai Fracture Zone
Clarion Fracture Zone
Clipperton Fracture Zone
Mendocino Fracture Zone
Monterey Fan
Tuffo Abyssal Plain
Baja Calif.
Spits
MEXICO
Singapore
Thailand
Cambodia
Gulf of Thailand
Sulawesi
Celebes Sea
Taiwan
Ryukyu Is.
Honshu
Kyushu
Sikhote Alin
Kamchatka
Aleutian Is.
Hawaiian Is.
Midway Is.
Johnston I.
Kingman Reef
Palmyra I.
Christmas I.
Fanning I.
Canton I.
Enderbury I.
Phoenix Is.
Tokelau Is.
Samoa Is.
Tonga Is.
Fiji Is.
Solomon Is.
New Hebrides
New Caledonia
Loyalty Is.
Norfolk I.
New Zealand
Tasman Sea
Coral Sea
Gulf of Alaska
Aleutian Trench
Kuril Trench
Japan Trench
Ryukyu Trench
Philippine Trench
Mariana Trench
Tonga Trench
Kermadec Trench
Peru-Chile Trench
Middle America Trench
Galapagos Rift
East Pacific Rise
Chile Rise
Easter I.
Juan Fernandez Is.
Galapagos Is.
Cocos I.
Malpelo I.
Colombia
Ecuador
Peru
Chile
Panama
Costa Rica
Nicaragua
Guatemala
Mexico
Baja California
Gulf of California
Revillagigedo Is.
Clipperton I.
Socorro I.
Guadalupe I.
Cedros I.
San Clemente I.
Santa Catalina I.
San Nicolas I.
Santa Barbara I.
Santa Rosa I.
Santa Cruz I.
San Miguel I.
San Francisco
Monterey
Point Arena
Cape Mendocino
Cape Flattery
Vancouver I.
Queen Charlotte Is.
Alaska
Yukon
Mackenzie
Great Slave Lake
Great Bear Lake
Hudson Bay
Baffin I.
Greenland
Iceland
Norway
Sweden
Finland
Russia
Siberia
Lena R.
Yenisey R.
Ob R.
Volga R.
Ural Mts.
Caspian Sea
Black Sea
Mediterranean Sea
Europe
Africa
Asia
Australia
Indonesia
Borneo
Sumatra
Java
New Guinea
Philippines
Luzon
Mindanao
Taiwan
Japan
Korea
China
India
Pakistan
Afghanistan
Iran
Iraq
Saudi Arabia
Yemen
Oman
Persian Gulf
Red Sea
Gulf of Aden
Arabian Sea
Bay of Bengal
Andaman Is.
Nicobar Is.
Sri Lanka
Maldives
Laccadive Is.
Madagascar
Mozambique Channel
Somalia
Ethiopia
Kenya
Tanzania
Mozambique
South Africa
Namibia
Angola
Zaire
Nigeria
Ghana
Ivory Coast
Liberia
Sierra Leone
Guinea
Senegal
Mauritania
Morocco
Algeria
Tunisia
Libya
Egypt
Sudan
Chad
Niger
Mali
Burkina Faso
Togo
Benin
Cameroon
Gabon
Congo
Zambia
Zimbabwe
Botswana
Lesotho
Swaziland
Malawi
Uganda
Rwanda
Burundi
Ethiopia
Somalia
Kenya
Tanzania
Mozambique
South Africa
Namibia
Angola
Zaire
Nigeria
Ghana
Ivory Coast
Liberia
Sierra Leone
Guinea
Senegal
Mauritania
Morocco
Algeria
Tunisia
Libya
Egypt
Sudan
Chad
Niger
Mali
Burkina Faso
Togo
Benin
Cameroon
Gabon
Congo
Zambia
Zimbabwe
Botswana
Lesotho
Swaziland
Malawi
Uganda
Rwanda
Burundi

Figure 4

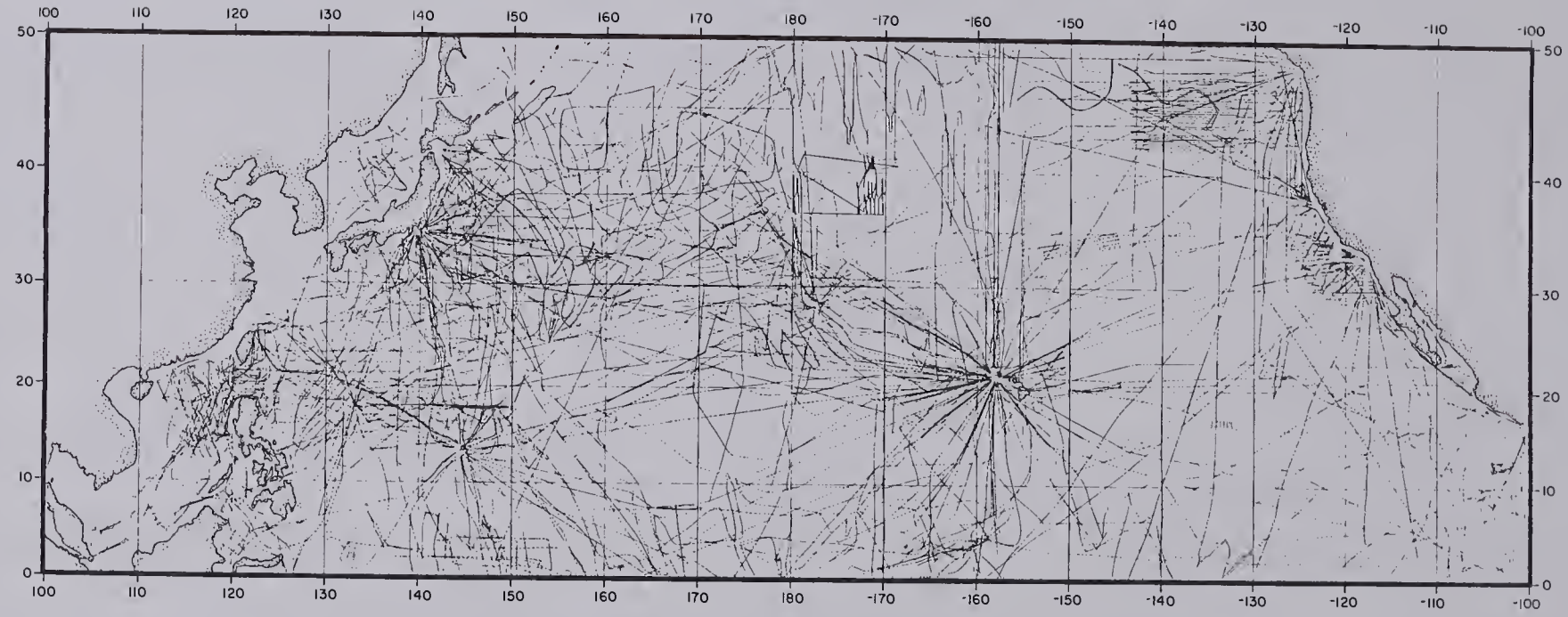
100
110
120
130
140
150
160
170
180
-170
-160
-150
-140
-130
-120
-110
-100
50
40
30
20
10
0

Figure 5

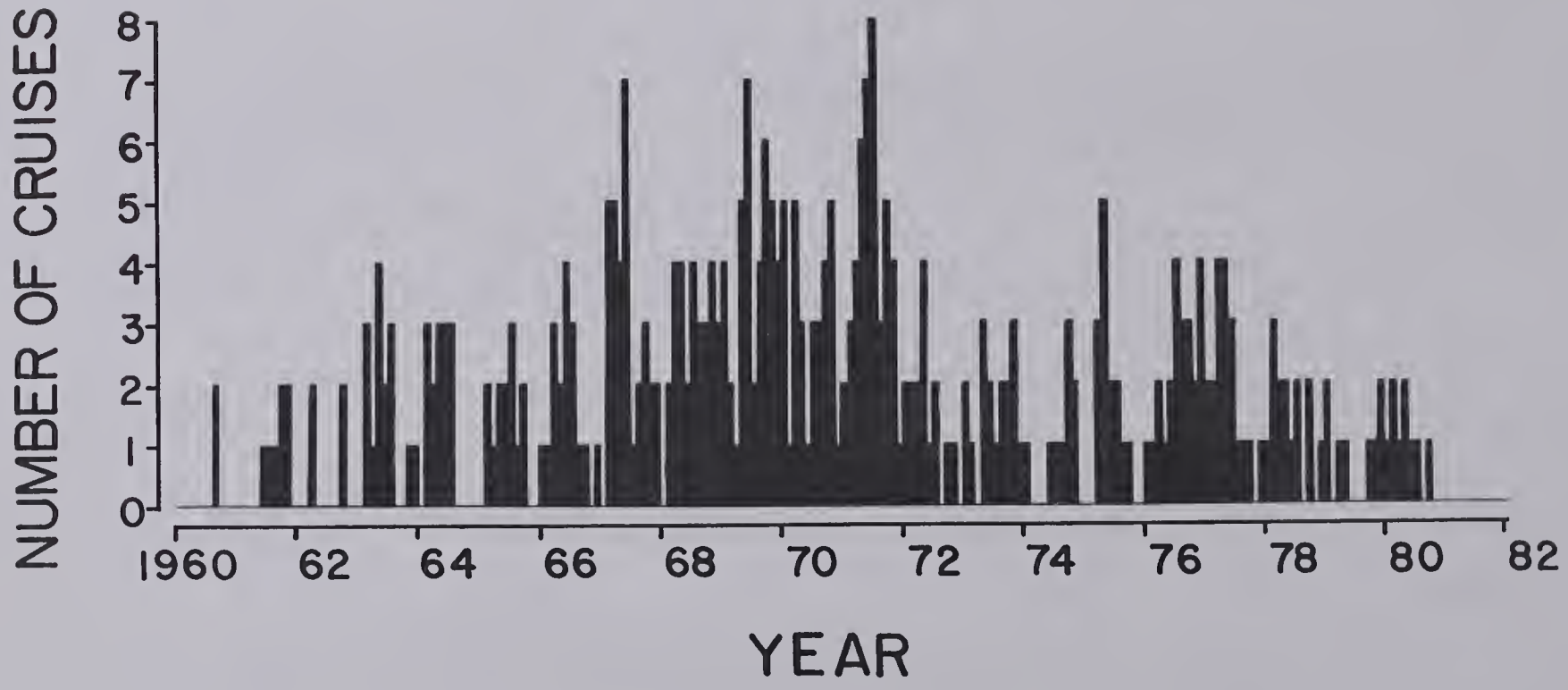
NUMBER OF CRUISES
0
1
2
3
4
5
6
7
8
1960
62
64
66
68
70
72
74
76
78
80
82
YEAR

Figure 6

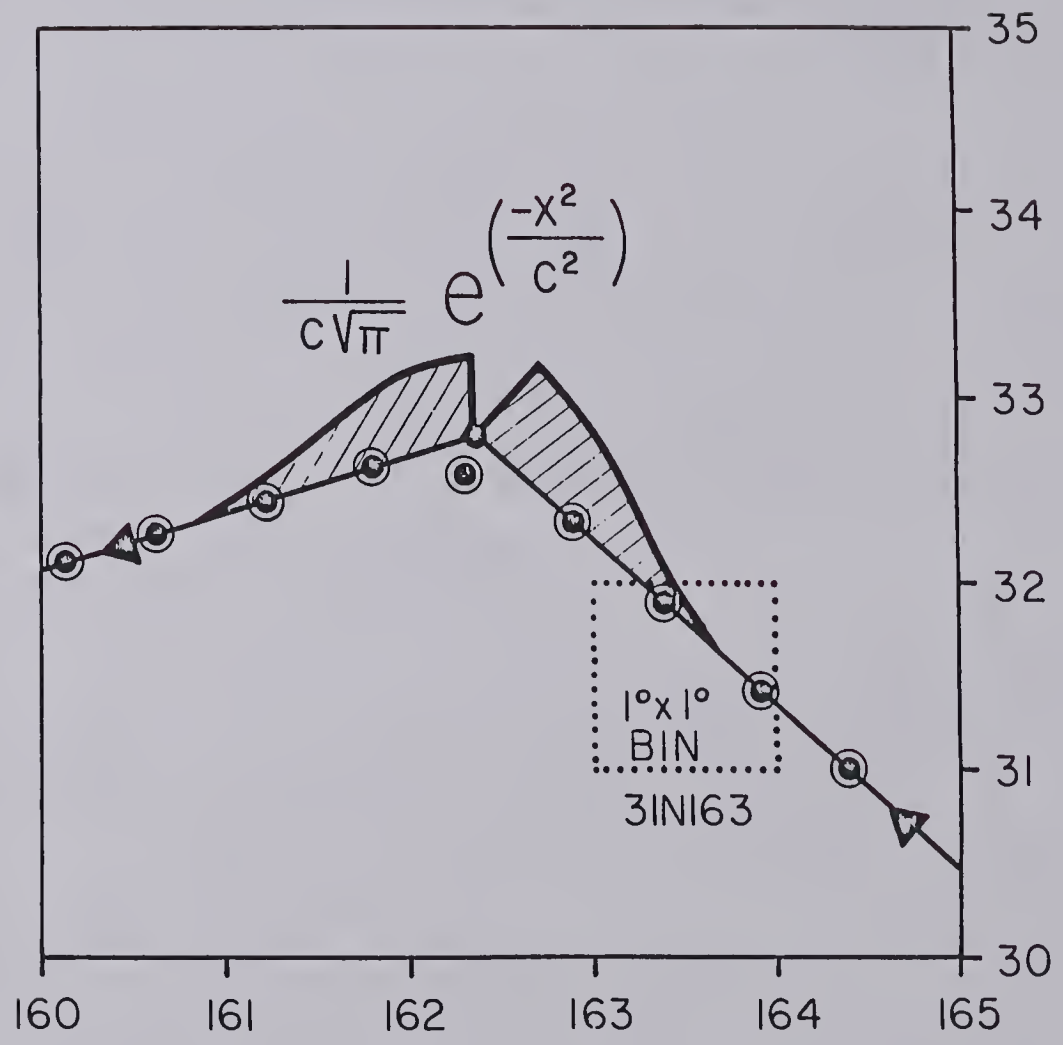
$\frac{1}{c\sqrt{\pi}}\, e^{\left(\frac{-x^2}{c^2}\right)}$
1°x1°
BIN
3IN163
35
34
33
32
31
30
160
161
162
163
164
165

Figure 7

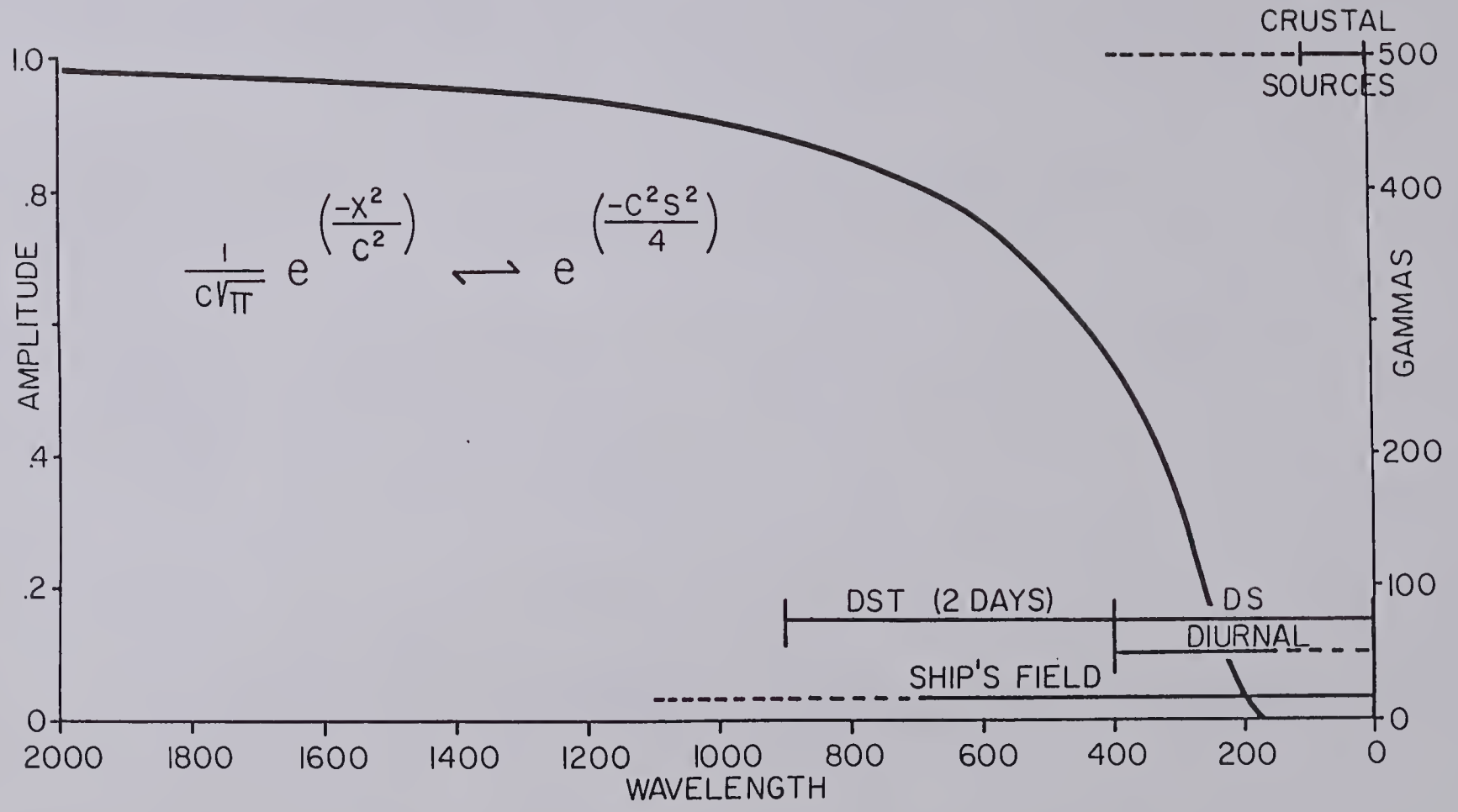
CRUSTAL
SOURCES
500
400
200
100
0
GAMMAS
1.0
.8
.4
.2
0
AMPLITUDE
$\frac{1}{c\sqrt{\pi}} e^{\left(\frac{-x^2}{c^2}\right)} \rightleftharpoons e^{\left(\frac{-c^2 s^2}{4}\right)}$
DST (2 DAYS)
DS
DIURNAL
SHIP'S FIELD
2000
1800
1600
1400
1200
1000
800
600
400
200
0
WAVELENGTH

Figure 8

Magnetic indices *Kp*, *ap*, and *Dst* for the magnetic storm of February 15–17, 1979.

A comparison of the rate of evolution of $Dst(H)$ and the double amplitude of the first harmonic component of $DS(H)$ at mean geomagnetic latitude 30°. (After *Sugiura and Chapman*, 1960.)

Figure 9

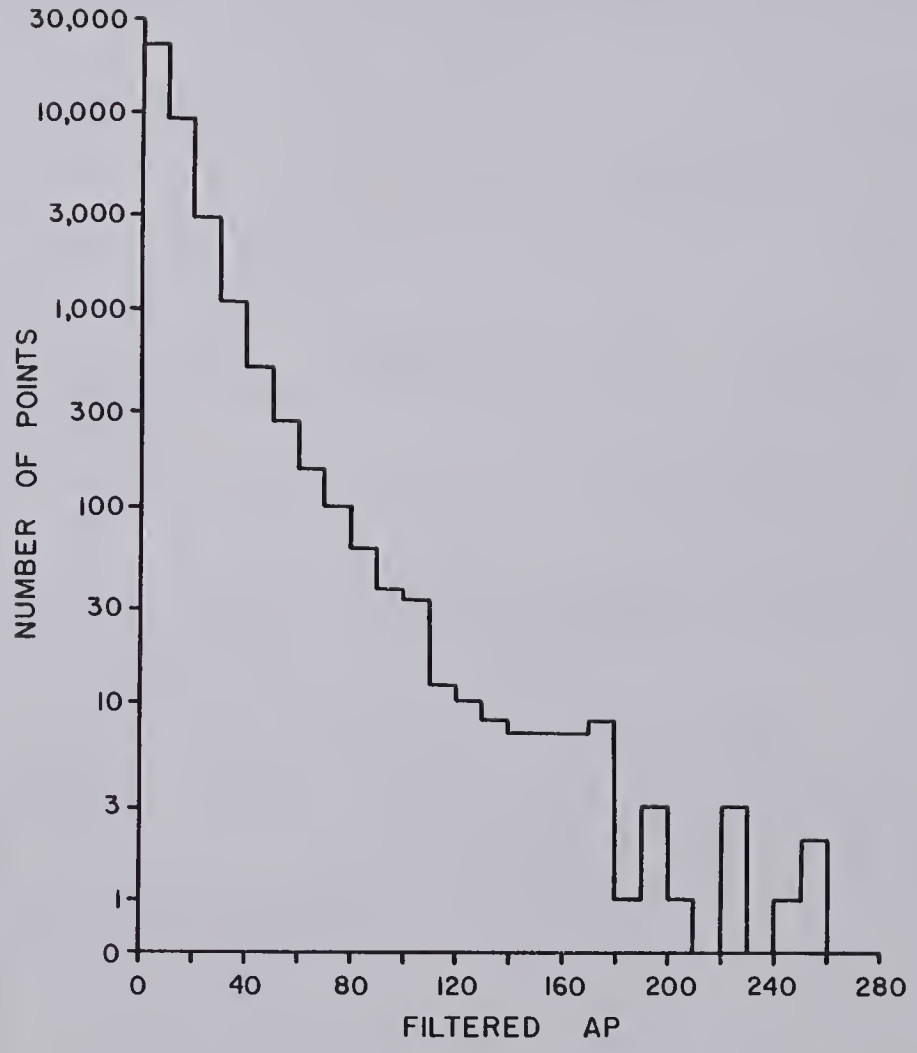
30,000
10,000
3,000
1,000
300
100
30
10
3
1
0
NUMBER OF POINTS
0
40
80
120
160
200
240
280
FILTERED AP

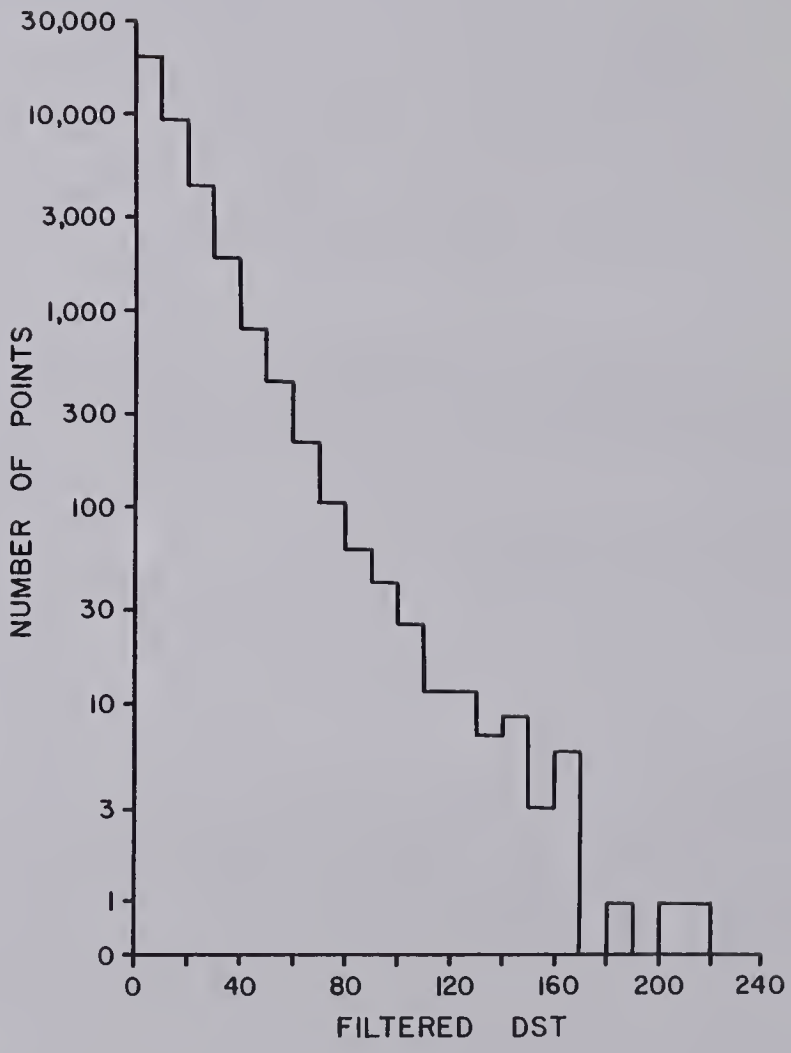
30,000
10,000
3,000
1,000
300
100
30
10
3
1
0
NUMBER OF POINTS
0
40
80
120
160
200
240
FILTERED DST

Figure 10

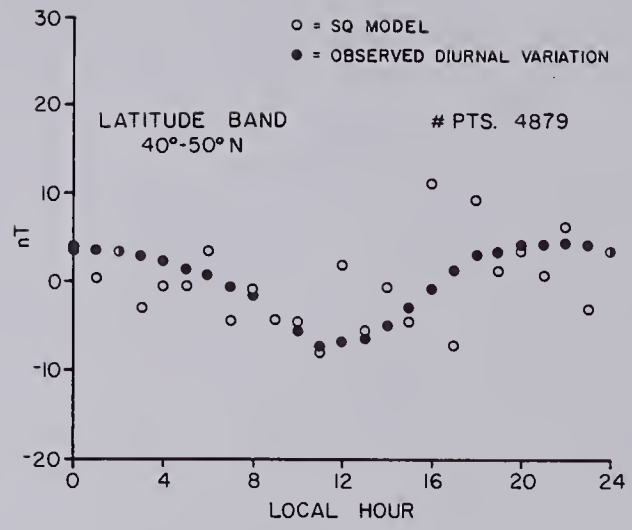
○ = SQ MODEL
● = OBSERVED DIURNAL VARIATION
LATITUDE BAND
40°-50° N
PTS. 4879
nT
LOCAL HOUR

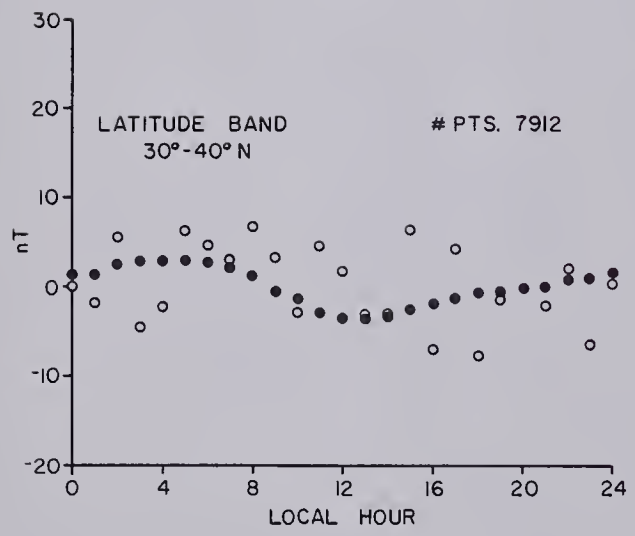
LATITUDE BAND
30°-40° N
PTS. 7912
nT
LOCAL HOUR

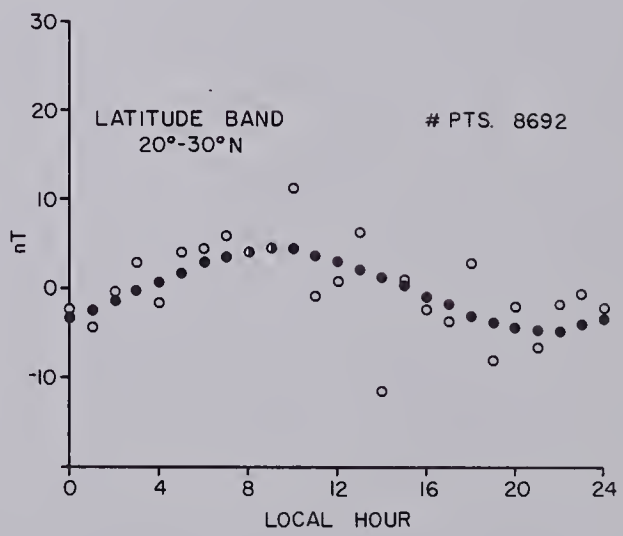
LATITUDE BAND
20°-30° N
PTS. 8692
nT
LOCAL HOUR

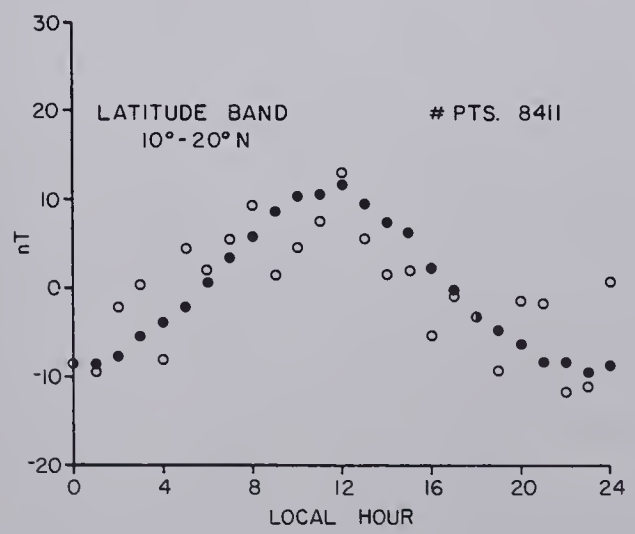
LATITUDE BAND
10°-20° N
PTS. 8411
nT
LOCAL HOUR

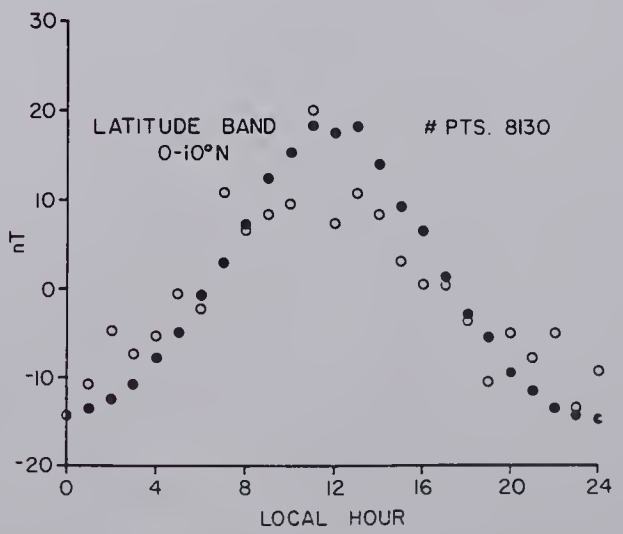
LATITUDE BAND
0-10° N
PTS. 8130
nT
LOCAL HOUR

Figure 11

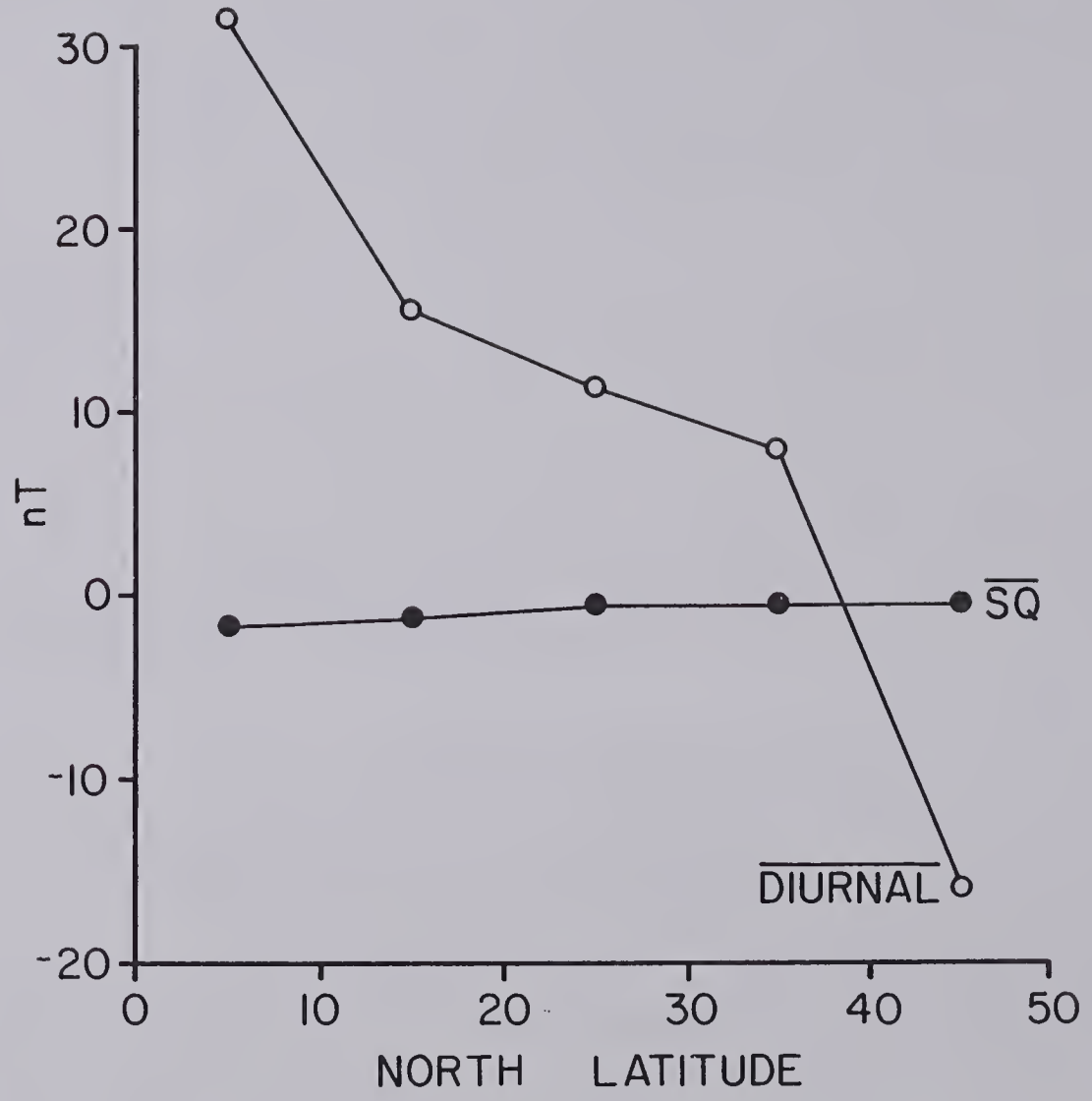

Figure 12

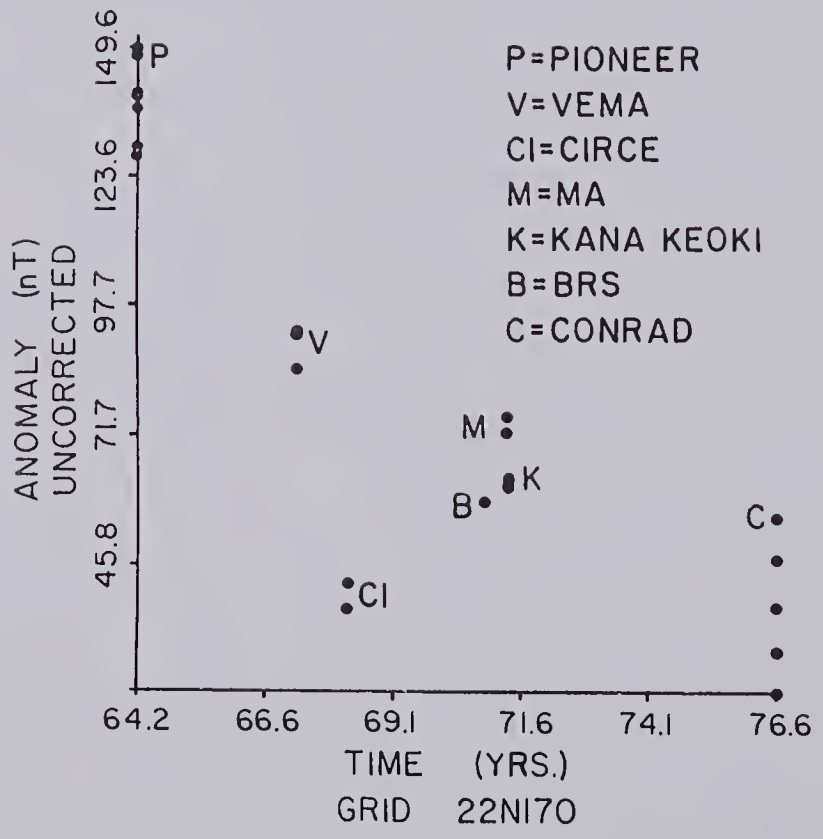
ANOMALY (nT)
UNCORRECTED
149.6
123.6
97.7
71.7
45.8
P=PIONEER
V=VEMA
CI=CIRCE
M=MA
K=KANA KEOKI
B=BRS
C=CONRAD
P
V
M
K
B
CI
C
64.2
66.6
69.1
71.6
74.1
76.6
TIME (YRS.)
GRID 22NI70

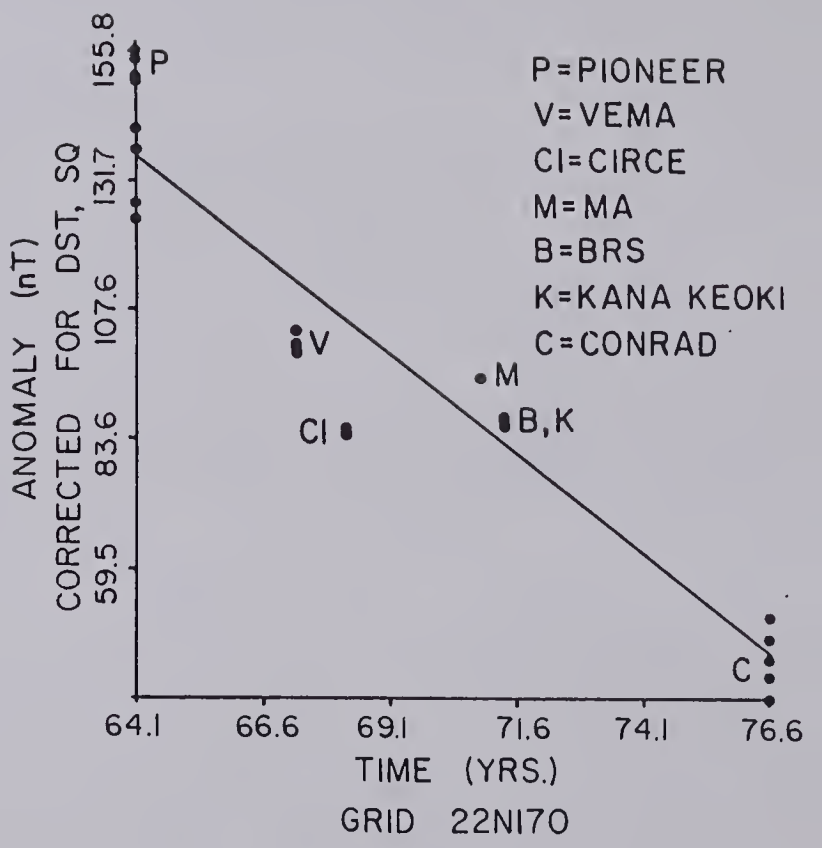
ANOMALY (nT)
CORRECTED FOR DST, SQ
155.8
131.7
107.6
83.6
59.5
P=PIONEER
V=VEMA
CI=CIRCE
M=MA
B=BRS
K=KANA KEOKI
C=CONRAD
P
V
M
B,K
CI
C
64.1
66.6
69.1
71.6
74.1
76.6
TIME (YRS.)
GRID 22NI70

Figure 13

SECULAR VARIATION ANOMALY

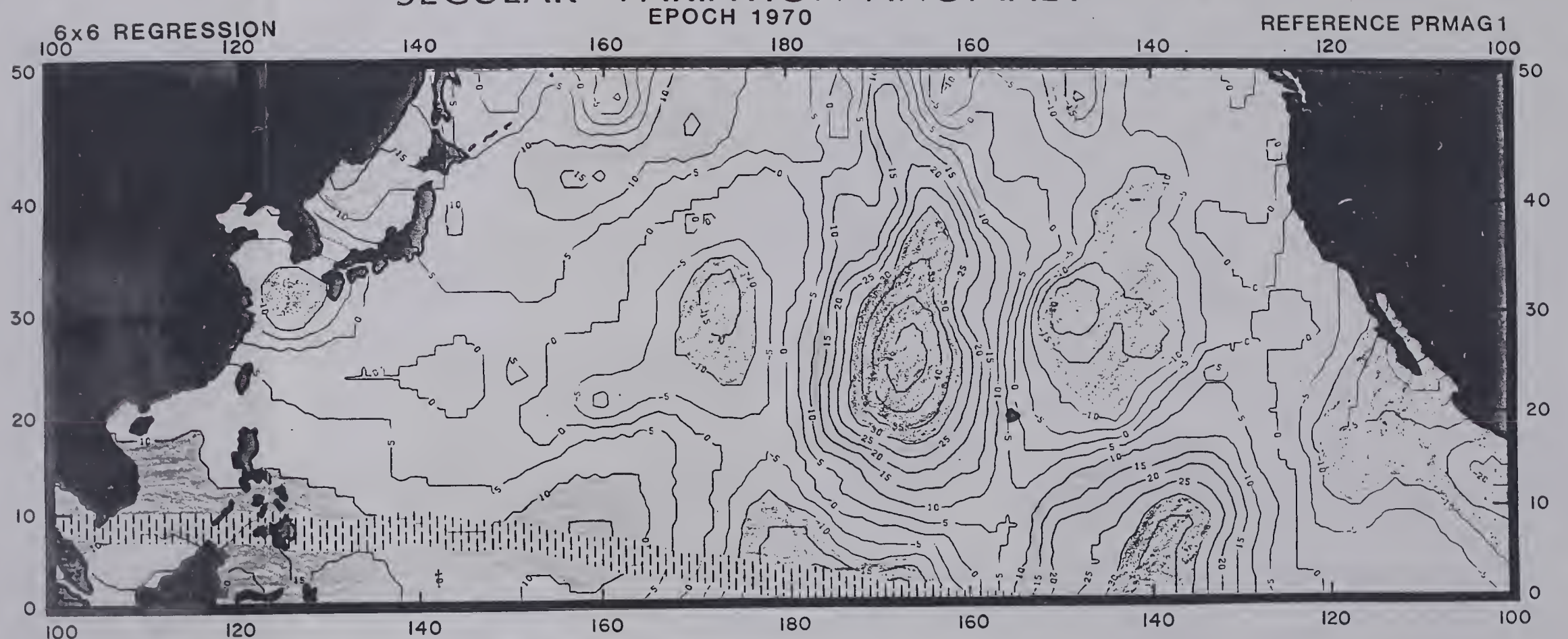

< -10 | -10 to 10 | 10 to 30 | > 30

UNITS: nT/yr

Figure 14

FILTERED SEA SURFACE ANOMALY

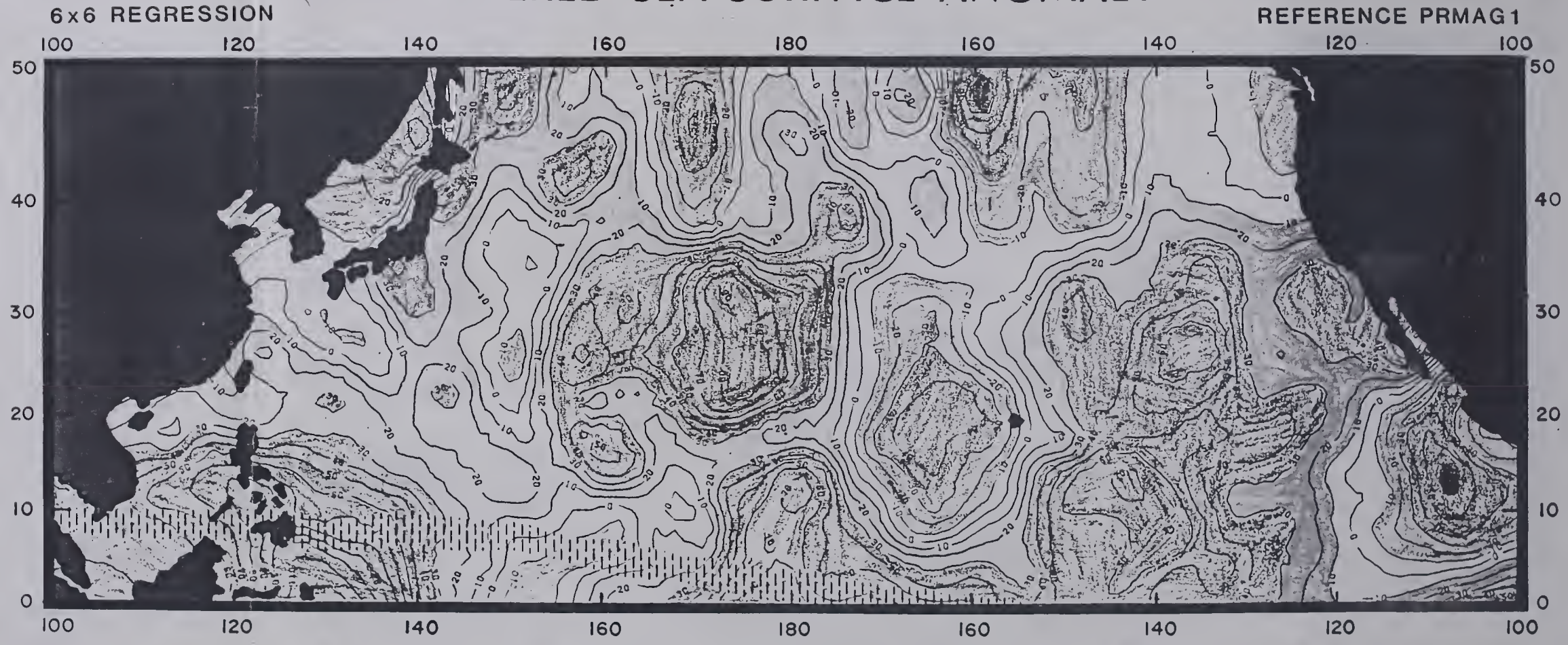

Figure 15

SOLOMON RISE
MARSHALL
GILBERT SEAMOUNTS
MID-PACIFIC
MAPMAKERS SEAMOUNTS
SHATSKY RISE
HESS RISE
HAWAIIAN RIDGE
SEAMOUNTS
EMPEROR SEAMOUNT CHAIN
TROUGH
EMPEROR

Figure 16

SOLOMON RISE
MARSHALL
MID-PACIFIC
SEAMOUNTS
SEAMOUNTS
HAWAIIAN RIDGE
HESS RISE
EMPEROR TROUGH
EMPEROR SEAMOUNT CHAIN
SHATSKY RISE
SEAMOUNTS
150
160
170
180
10
20
30
40
50

Figure 17

EMPEROR ANOMALY
MAGSAT TOTAL FIELD ANOMALY

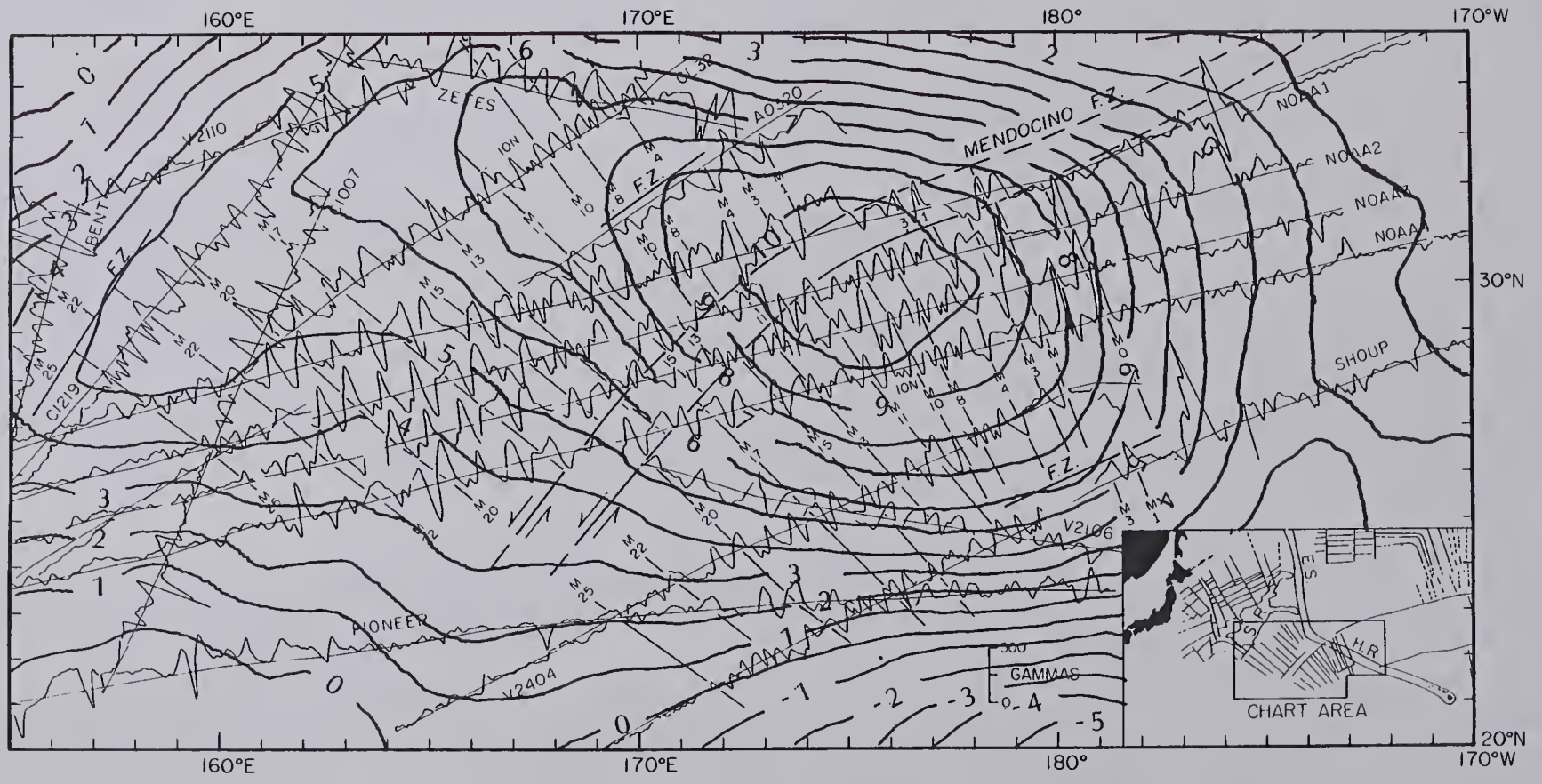

CONTOUR INTERVAL : 1 nT

Figure 18

EMPEROR ANOMALY
FILTERED SEA SURFACE TOTAL FIELD

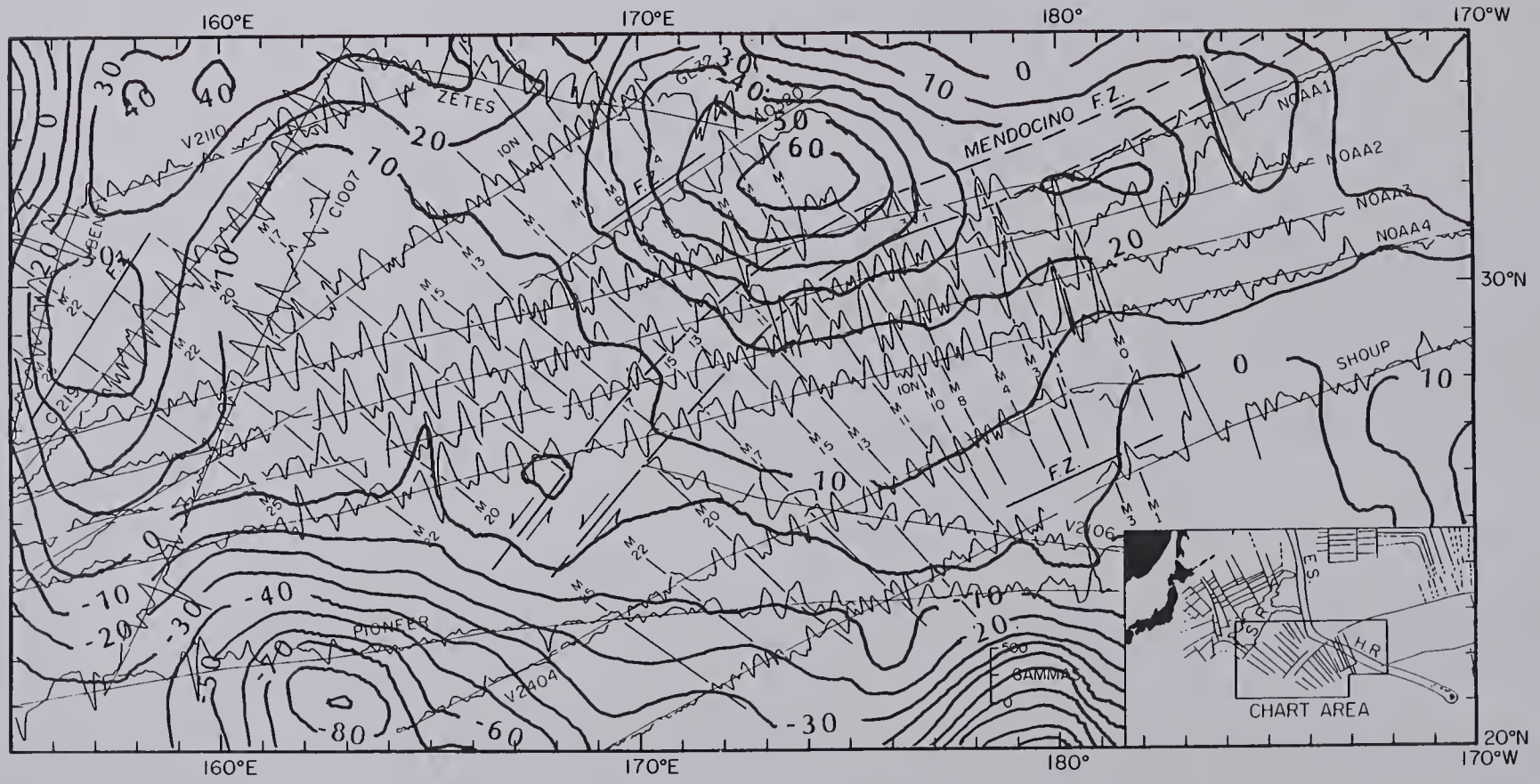

CONTOUR INTERVAL : 10 nT

Figure 19

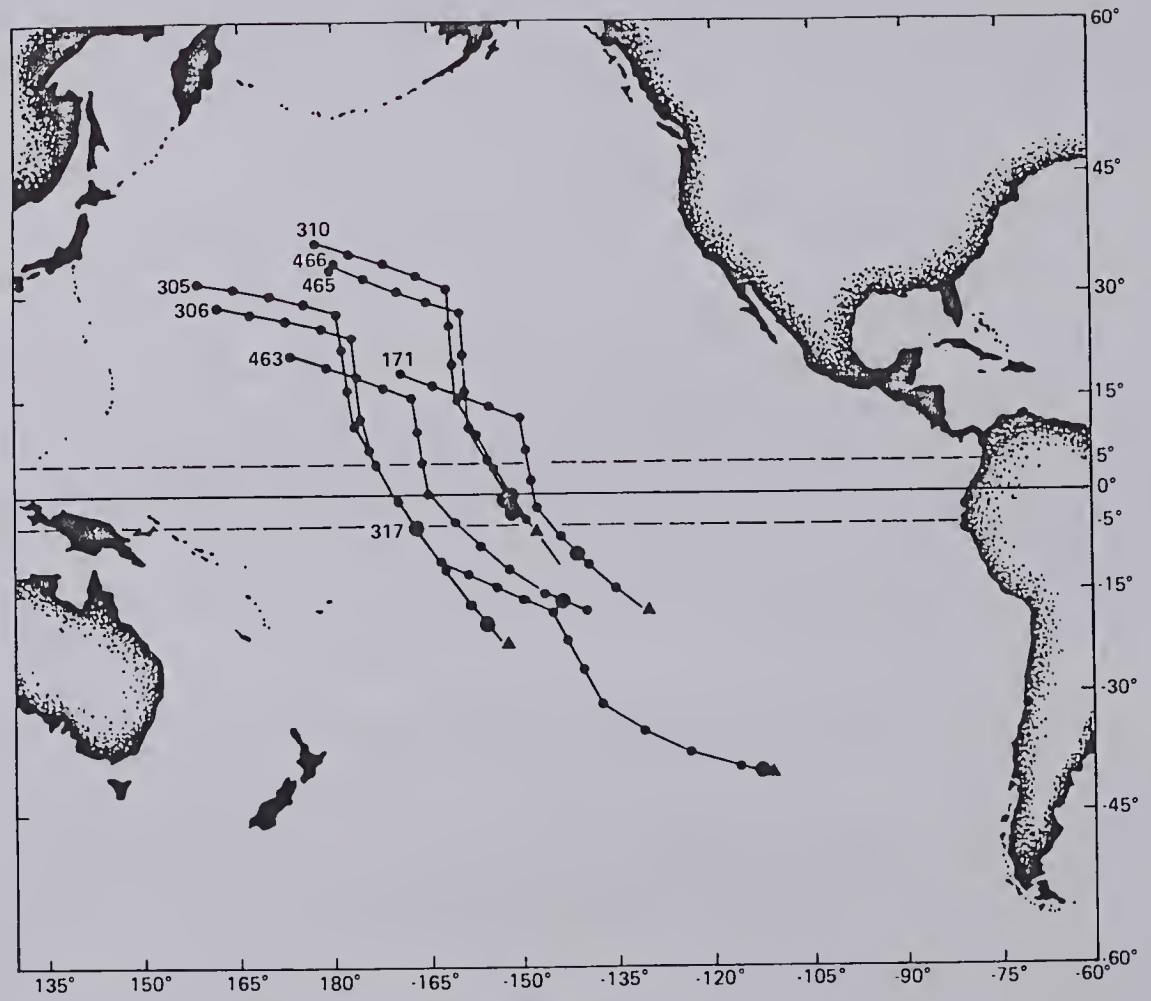
310
466
465
305
306
463
171
317
60°
45°
30°
15°
5°
0°
-5°
-15°
-30°
-45°
-60°
135°
150°
165°
180°
-165°
-150°
-135°
-120°
-105°
-90°
-75°
-60°

Figure 20

Figure 21

SHATSKY RISE
AZZ: 315
REMANENT
INDUCED
HAWAIIAN SMTS.
AZZ: 30
MARSHALL GILBERT SMTS.
AZZ: 30
REMANENT
INDUCED
HESS RISE
AZZ: 355
MID-PACIFIC SMTS.
AZZ: 0
REMANENT
INDUCED
EMPEROR SMTS.
AZZ: 90
SCALE
300 nT
10 nT
400 km
2
6
km
12

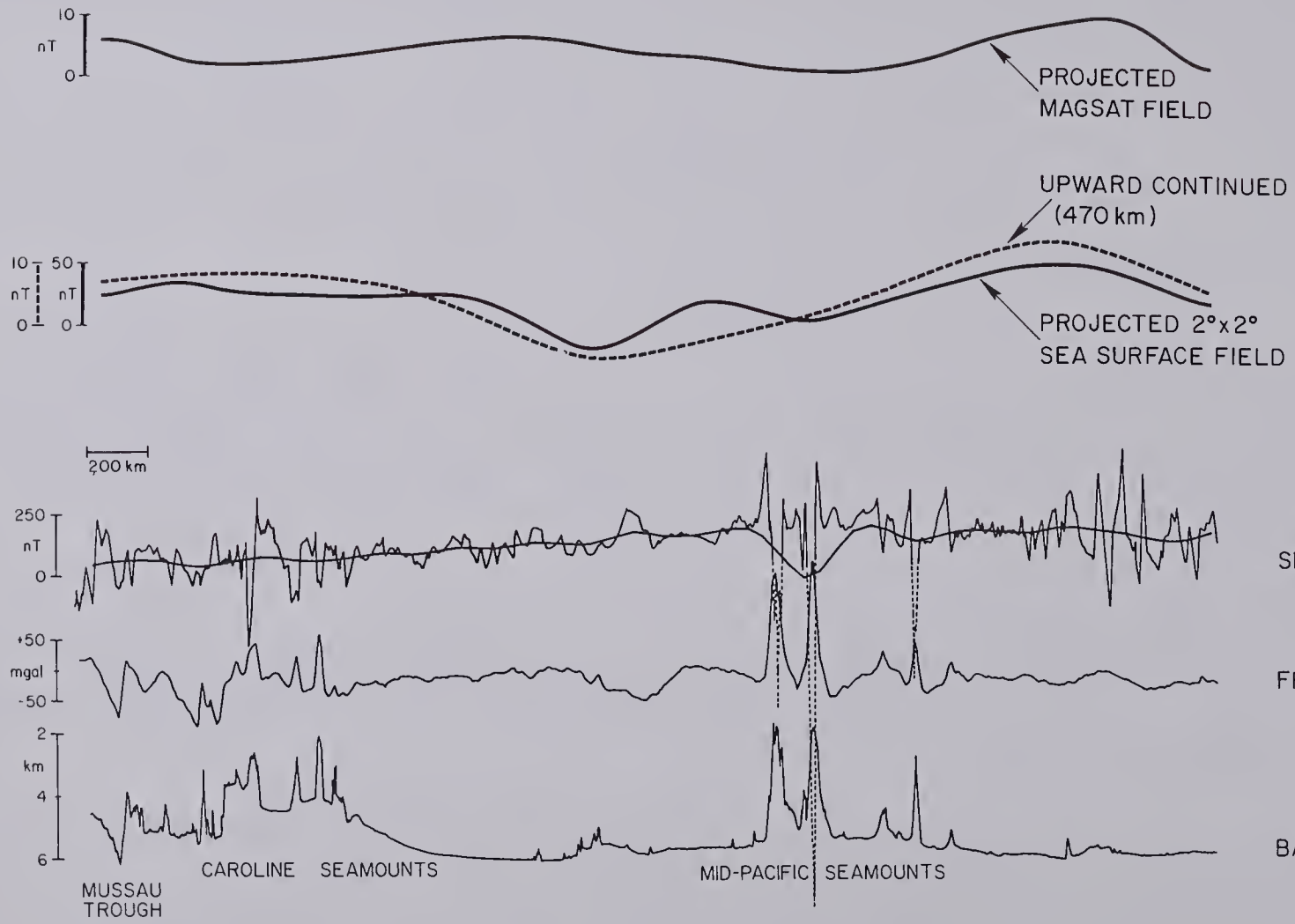
10
nT
0
PROJECTED
MAGSAT FIELD
UPWARD CONTINUED
(470 km)
10
nT
0
50
nT
0
PROJECTED 2°x2°
SEA SURFACE FIELD
200 km
250
nT
0
CONRAD 1007
OBSERVED AND
SMOOTHED MAGNETICS
+50
mgal
-50
FREE-AIR GRAVITY
2
km
4
6
BATHYMETRY
MUSSAU
TROUGH
CAROLINE SEAMOUNTS
MID-PACIFIC SEAMOUNTS

Figure 22

120
130
140
150
45
40
30
20
10
0
JAPAN
SEA
JAPAN TRENCH
BONIN TRENCH
SHIKOKU BASIN
DAITO RIDGE
RYUKYU TRENCH
OKI DAITO RIDGE
WEST PHILIPPINE BASIN
KYUSHU-PALAU RIDGE
PARECE-VELA BASIN
WEST MARIANA RIDGE
MARIANA TRENCH
PHILIPPINE TRENCH
CAROLINE RIDGE
CAROLINE BASIN
EAURIPIK RISE

Figure 23

120
130
140
150
45
40
30
20
10
0
JAPAN
SEA
HONSHU
JAPAN
TRENCH
BONIN
TRENCH
IZU-OGASAWARA
TRENCH
DAITO RIDGE
OKI DAITO RIDGE
RYUKYU
TAIWAN
WEST
PHILIPPINE
BASIN
PHILIPPINE
TRENCH
KYUSHU-PALAU
RIDGE
PARECE VELA
BASIN
WEST
MARIANA
RIDGE
MARIANA
TRENCH
CAROLINE RIDGE
BASIN
CAROLINE
RIDGE
EAURIPIK RISE

Figure 24

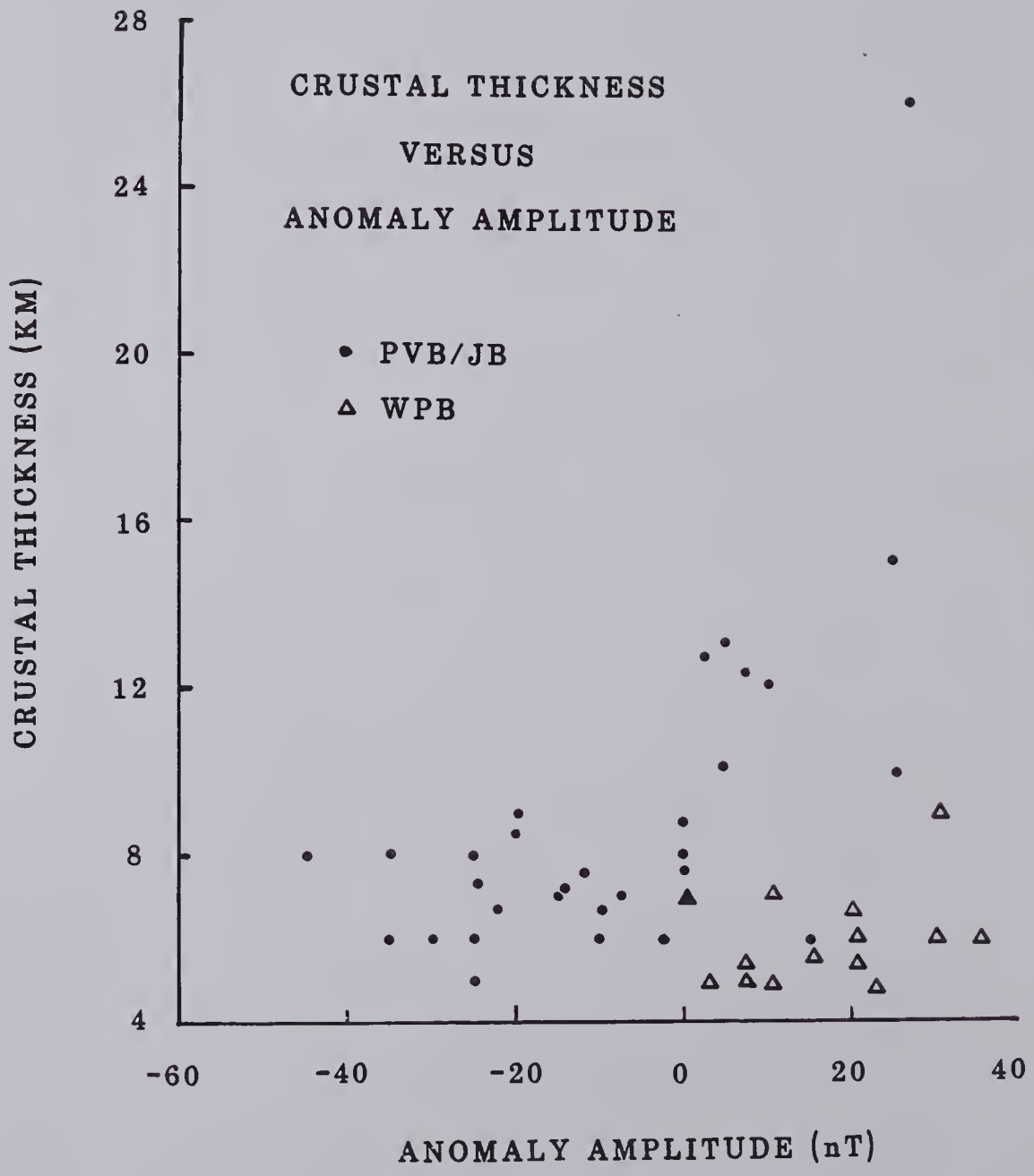
CRUSTAL THICKNESS
VERSUS
ANOMALY AMPLITUDE
• PVB/JB
△ WPB
CRUSTAL THICKNESS (KM)
28
24
20
16
12
8
4
-60
-40
-20
0
20
40
ANOMALY AMPLITUDE (nT)

Figure 25a

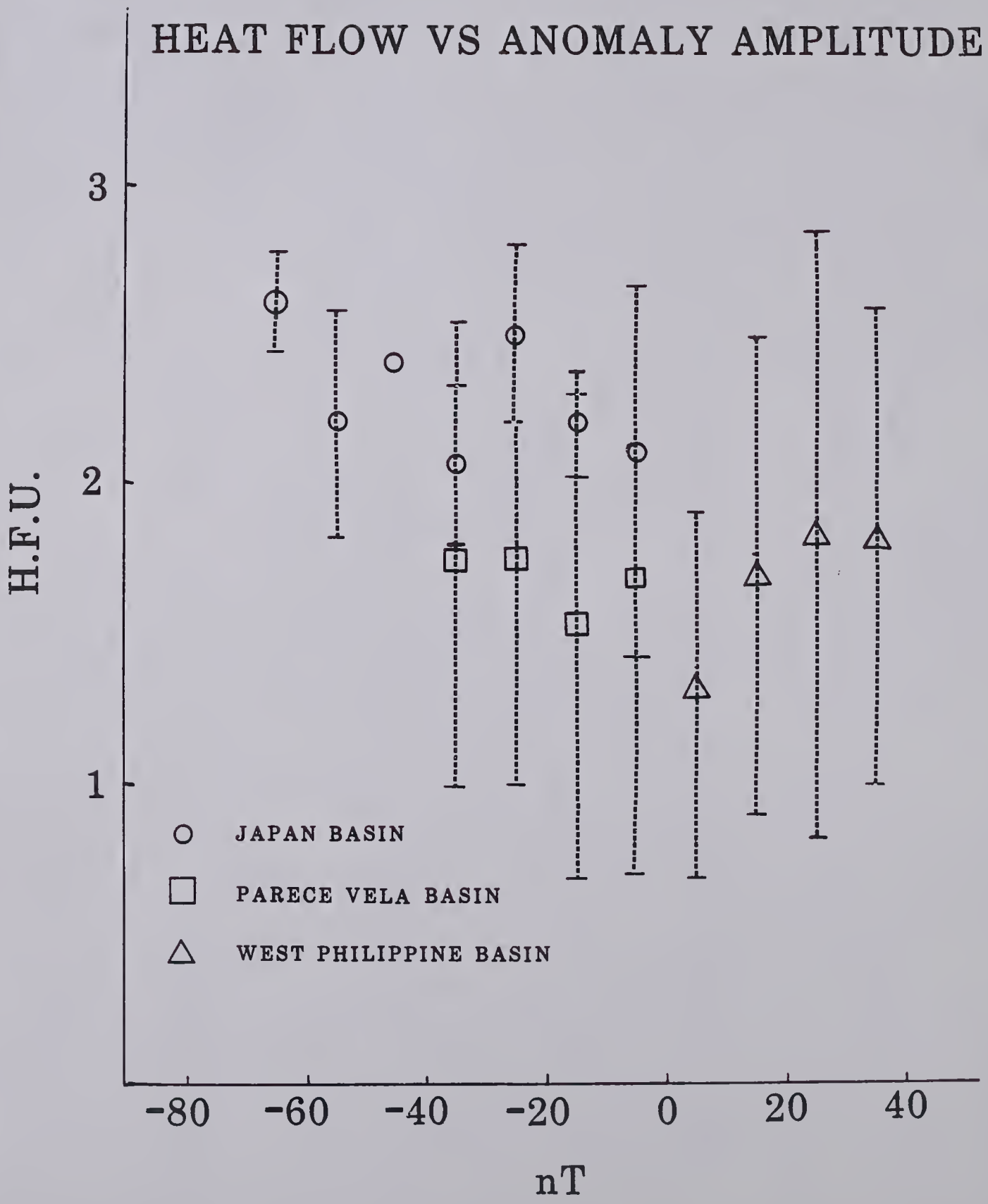
HEAT FLOW VS ANOMALY AMPLITUDE
H.F.U.
3
2
1
-80
-60
-40
-20
0
20
40
nT
JAPAN BASIN
PARECE VELA BASIN
WEST PHILIPPINE BASIN

Figure 25 b

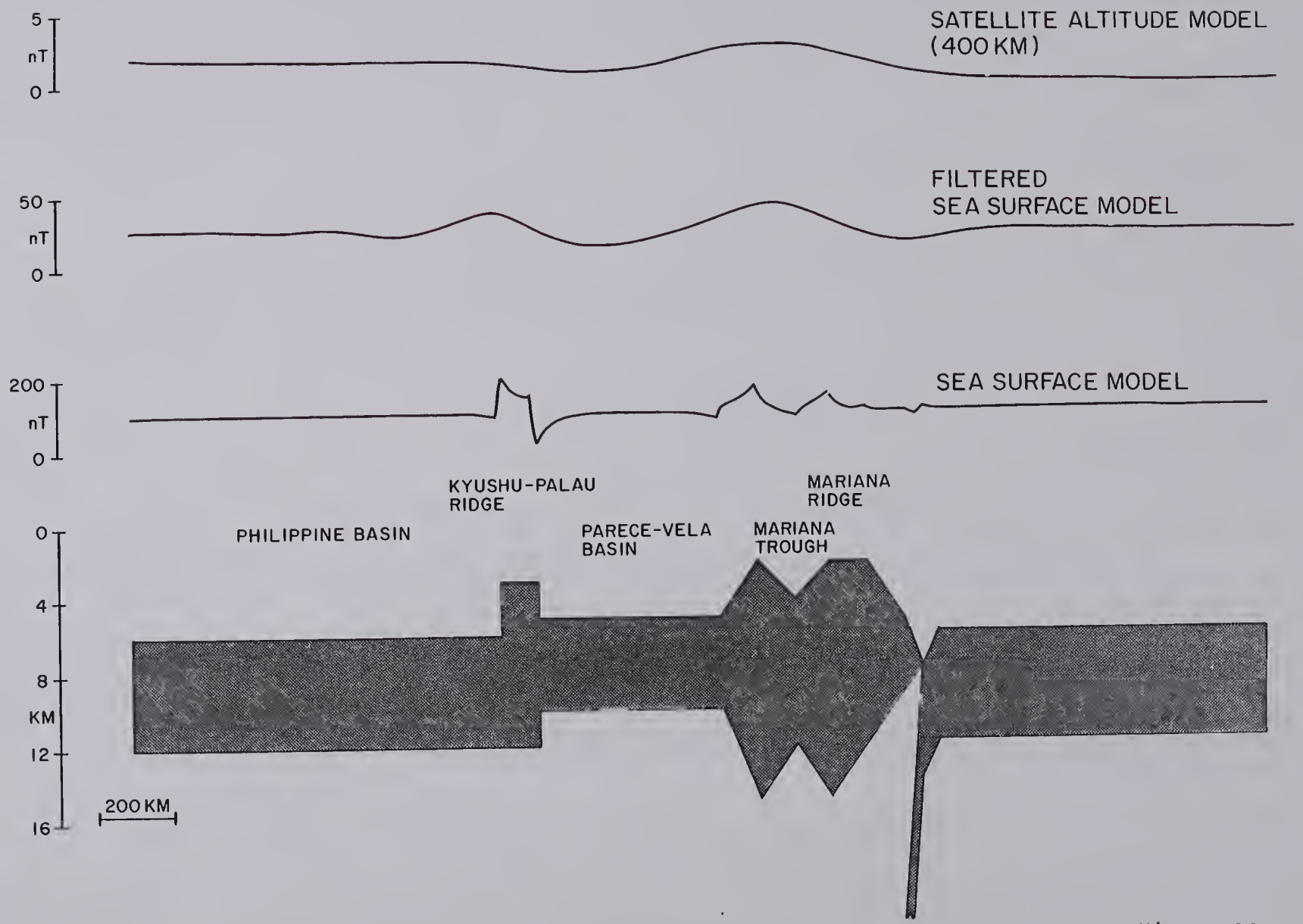
5
nT
0
SATELLITE ALTITUDE MODEL
(400 KM)
50
nT
0
FILTERED
SEA SURFACE MODEL
200
nT
0
SEA SURFACE MODEL
KYUSHU-PALAU
RIDGE
MARIANA
RIDGE
PHILIPPINE BASIN
PARECE-VELA
BASIN
MARIANA
TROUGH
0
4
8
KM
12
16
200 KM

Figure 26

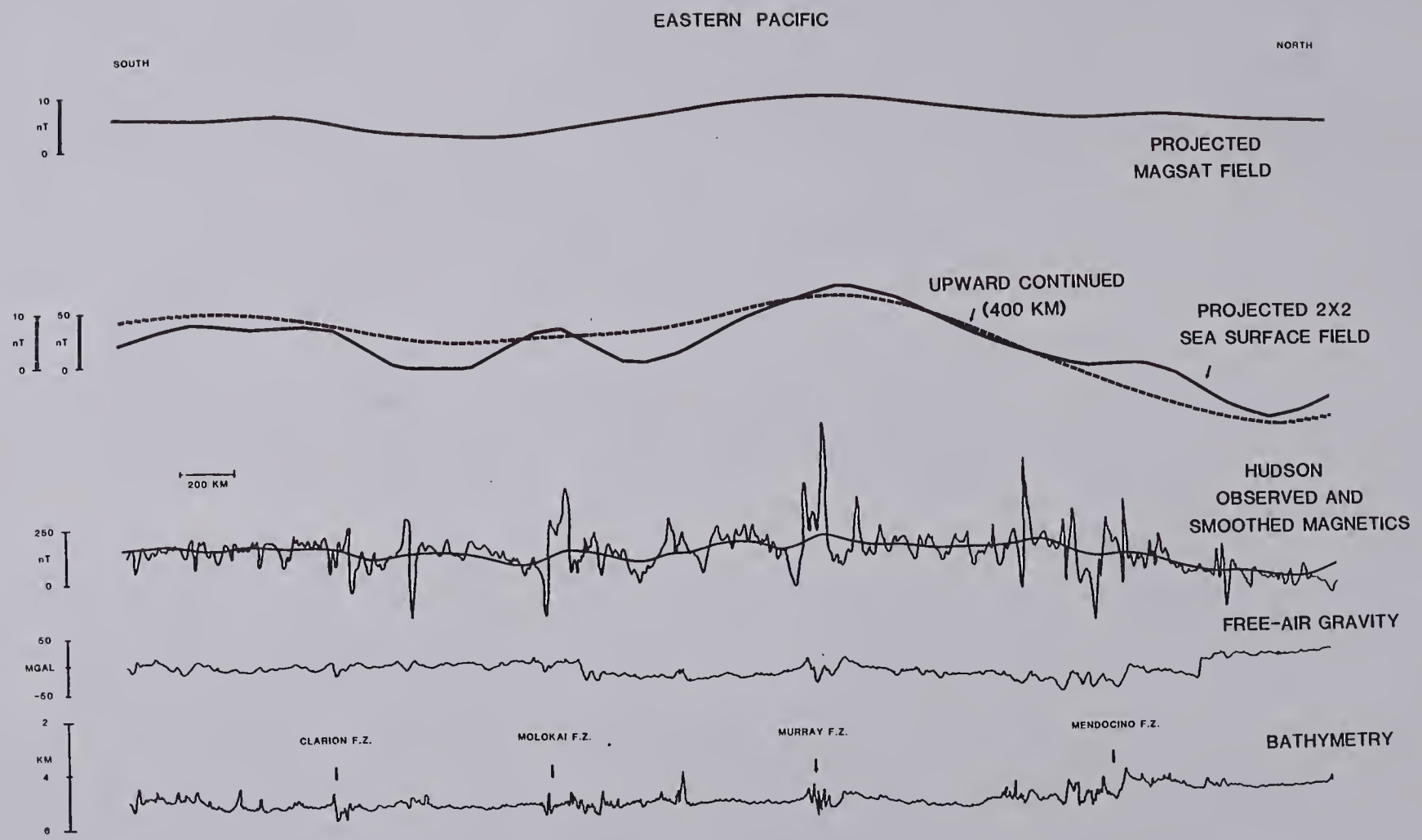
EASTERN PACIFIC
SOUTH
NORTH
10
nT
0
PROJECTED
MAGSAT FIELD
10
nT
0
50
nT
0
UPWARD CONTINUED
(400 KM)
PROJECTED 2X2
SEA SURFACE FIELD
200 KM
HUDSON
OBSERVED AND
SMOOTHED MAGNETICS
250
nT
0
FREE-AIR GRAVITY
50
MGAL
-50
2
KM
4
6
CLARION F.Z.
MOLOKAI F.Z.
MURRAY F.Z.
MENDOCINO F.Z.
BATHYMETRY

Figure 27

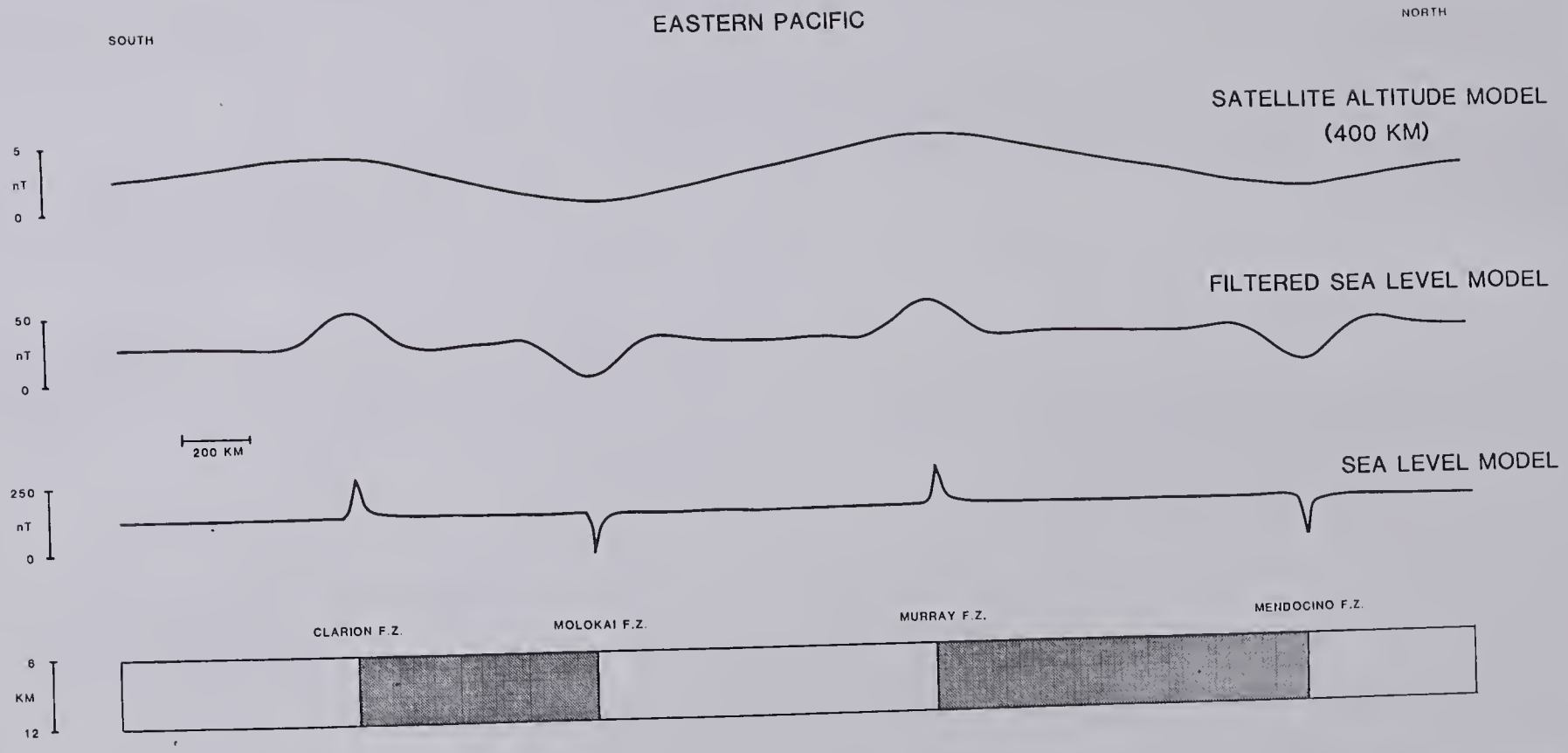

Figure 28